Tectonics

RESEARCH ARTICLE

10.1029/2020TC006633

Key Points:

- High resolution digital topography helps locate morphological indexes of active tectonics in Morocco
- Cosmogenic nuclides allow placing time constraints for landscape development in the Southern Rif Front
- The Southern Rif Front is an important geodynamic boundary with a non-negligible seismogenic potential

Correspondence to:

L. Siame,
siame@cerege.fr

Citation:

Agharroud, K., Siame, L. L., Ben Moussa, A., Bellier, O., Guillou, V., Fleury, J., & El Kharim, Y. (2021). Seismo-tectonic model for the Southern Pre-Rif border (Northern Morocco): Insights from morphochronology. *Tectonics*, *40*, e2020TC006633. https://doi.org/10.1029/2020TC006633

Received 25 NOV 2020
Accepted 27 MAR 2021

Seismo-Tectonic Model for the Southern Pre-Rif Border (Northern Morocco): Insights From Morphochronology

Kamal Agharroud[1], Lionel L. Siame[2], Abdelkhalak Ben Moussa[1], Olivier Bellier[2], Valéry Guillou[2], Jules Fleury[2], and Younes El Kharim[1]

[1]Département de Géologie, Faculté des Sciences de l'Université Abdelmalek Essaâdi, Tétouan, Morocco, [2]Aix Marseille Univ, CNRS, IRD, INRAE, Coll France, CEREGE, Aix-en-Provence, France

Abstract Located at the southern boundary of the Alpine chain in Morocco, the deformation front of the Southern Rif Mountains is a region of moderate tectonic activity, which makes it a good natural laboratory to understand whether, and how, low compressional strains are located on specific structures. Along the ≈80 km-long left-lateral, transpressive and reverse fault zone that runs at the toe of the Pre-Rif Ridges, an analysis of high-resolution digital topography provides new geomorphic lines of evidence supporting Quaternary activity along, 20 km-long fault segments. The fault zone can be divided into the Meknès and the Fès segments, which are constrained at depth by reactivated, NE-trending basement faults, delimitating paleo-grabens associated with the Late Triassic-Jurassic opening of the Atlantic Ocean. For selected sites, we used in situ-produced ^{36}Cl, ^{10}Be, and ^{26}Al and high-resolution topography to infer the timing of abandonment of fluvial markers, which suggest incision rates on the order of 0.6–2 mm/yr. Given their lengths, scaling laws suggest that the identified fault segments should root at about 7–12 km-depth, possibly reactivating former basement normal faults and making them potential seismogenic sources capable of generating M_w6+ earthquakes, with return times of the order of several hundreds of years. Our new morphochronological data set confirms that the Southern Rif deformation front is a key structure that may have accommodated most of the lateral extrusion of the Rif between the Nubia and Iberia tectonic plates.

Plain Language Summary In Morocco, the population may suffer from the dramatic consequences of earthquakes. Far from a tectonic plate boundary, it is not so easy to localize in the landscape the faults that might be responsible for a strong earthquake. In this article, we used high-resolution satellite imagery to study the active faults along the Pre-Rif Ridges, in Northern Morocco. We also applied a dating technique that uses the accumulation of some rare isotopes in the rock exposed to cosmic particles at the surface of the Earth. The combination of the two methods permits to estimate rates of river incisions and to convert them into rates of shortening and fault slip. This study contributes to the seismic hazard assessment of the faults close to Meknès and Fès cities.

1. Introduction

In intraplate tectonic regions characterized by moderate seismic activity, the recognition of active zones of deformation has long been a challenging task (e.g., Landgraf et al., 2017). Like Northern Africa, such regions are generally characterized by low hazard but high risk due to the concentrations highly vulnerable population and/or infrastructures (Moreno et al., 2004). Moreover, when low strain rates are combined with meteorological and anthropogenic overprints, the geomorphic signatures associated with active faults fade away as fault slip rates decrease. Consequently, diagnostic criteria established in areas of high strain rates may not be effectively applied. Furthermore, low-levels of seismic strain induce low displacement rates, which may be distributed over numerous fault segments rather than localized on a single fault. At the regional scale, such a distribution of the tectonic deformation can also obscure the seismogenic potential of any given single structure, as, for example, the La Rouvière Fault reactivation during the 2019 M_w 4.9 Le Teil Earthquake (Ritz et al., 2020), in southeastern France, which was previously considered as inactive (Jomard et al., 2017).

Part of the peri-Mediterranean Alpine chain surrounding the Alboran Sea, the Rif Mountain belt in Morocco is an area of moderate tectonic activity. Located within the diffuse convergence zone between the Nubia

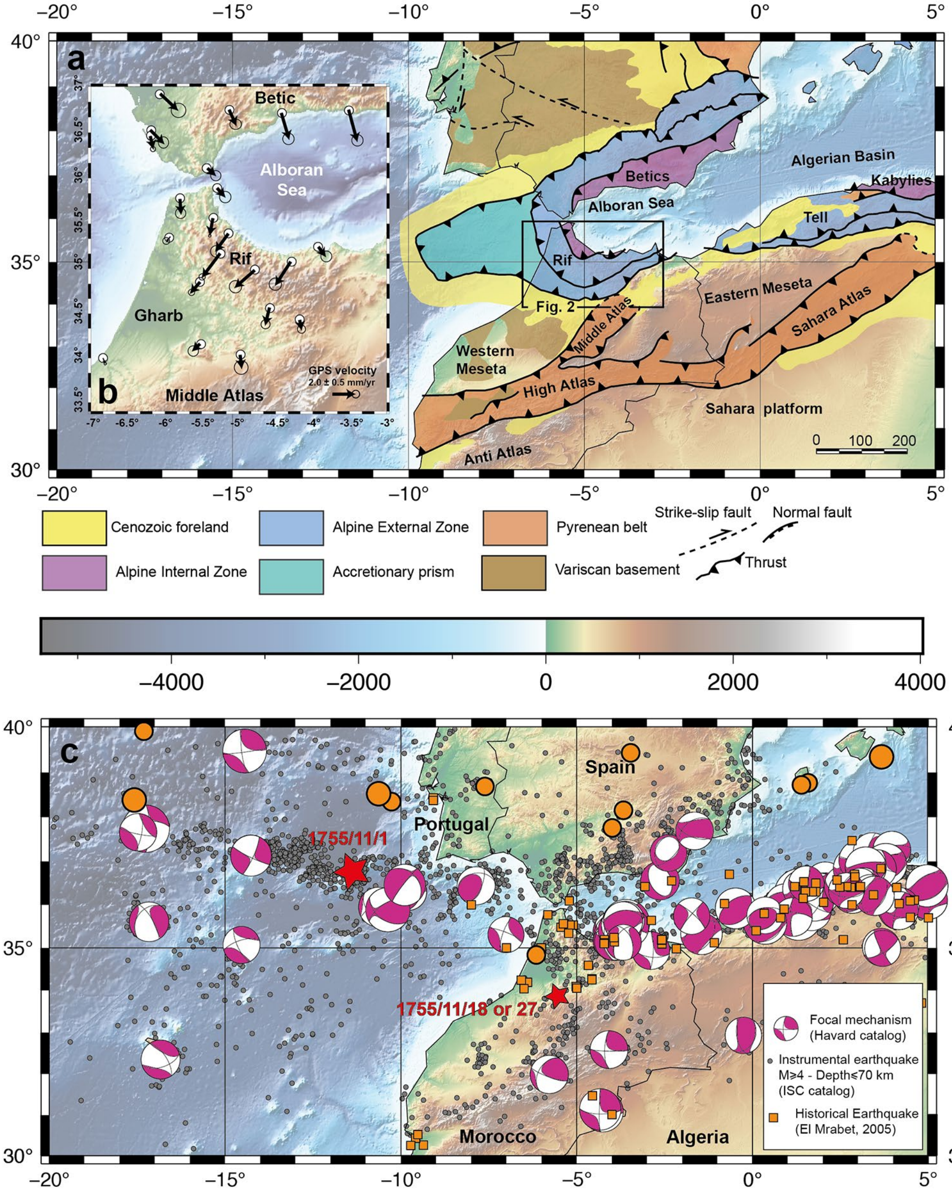

Figure 1. Geodynamic setting of Morocco. (a) Simplified map of the major Cenozoic structural trends centered on the Baetic-Rif Belt (modified after Etheve et al., 2016). (b) GPS-derived kinematics (relative to fixed Nubia) in northern Morocco and in the Alboran region (after Koulali et al., 2011). (c) Map of the instrumental (International Seismological Center, 2020), focal mechanisms (Harvard global centroid moment tensor catalog; e.g., Dziewonski et al., 1981; Ekström et al., 2012), and historical epicenters in the Maghreb region (El Mrabet, 2005). Red stars locate the epicenter areas of the November 1, 1755 and November 18 or 27, 1755 (see text for discussion).

and Iberia plates (Figure 1), this region experienced an oblique NW-SE shortening, with an estimated rate of about 4 mm/yr from global positioning system (GPS) data (McClusky et al., 2003) and geologically current plate motions (DeMets et al., 2010). At a first order, the present-day pattern of GPS displacement is in good agreement with the regional evidence for tectonic activity in Northern Morocco (Morel & Meghraoui, 1996) and in the Baetic ranges (Giaconia et al., 2012), which indicates a combination of crustal shortening in the Rif and extension in the Alboran Sea (e.g., Vernant et al., 2010). However, the southward-directed crustal motions observed in the Central Rif (Figure 1), almost normal to the direction of Nubia-Iberia plate motion, are incompatible with a simple two-plate model (Fadil et al., 2006; Pérouse et al., 2010; Vernant et al., 2010). This particular situation is still a matter of debate and models involving complex relationship between

10.1029/2020TC006633

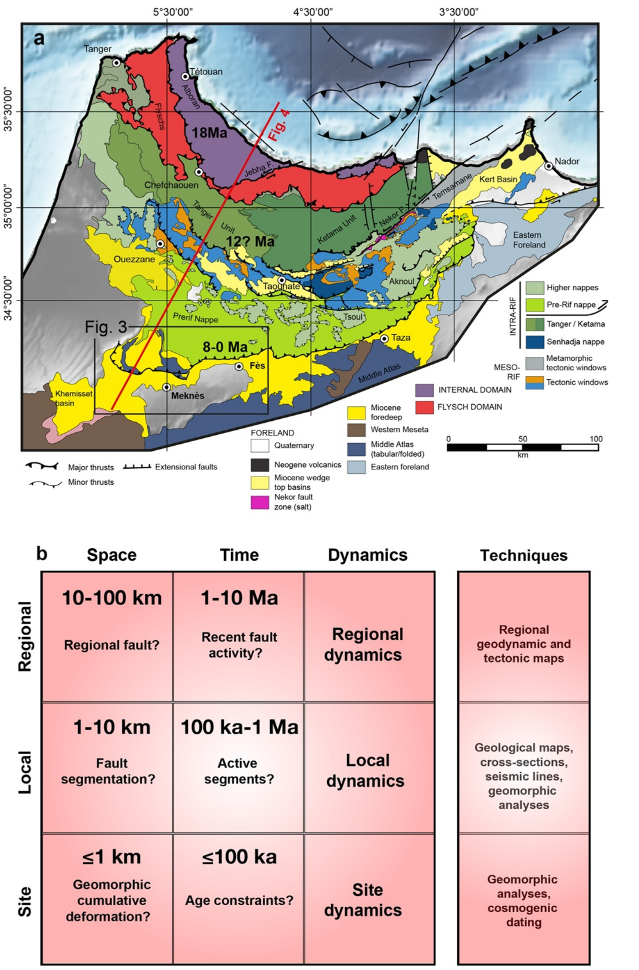

Figure 2. (a) Structural map of the main tectonic units composing the Rif Mountains in northern Morocco (modified after Chalouan et al., 2008; Gimeno-Vives et al., 2020; Suter, 1980), and showing the period of activity of the main boundary thrusts (after Abbassi et al., 2020). The open box and the red line locate the map shown in Figure 3a and the crustal-scale cross-section shown in Figure 4a, respectively. (b) Principle of matrix organization used to define a set of diagnostic criteria regarding fault activity in moderate domains of tectonic deformation. The fourth column lists the different types of data that were used in this study to cope with the different spatial and temporal scales (adapted from Siame & Sébrier, 2004).

mantle processes and crustal tectonics have been put forward such as, among others, oceanic lithosphere slab rollback or slab break-off of a subducting continental lithosphere (e.g., Bezada et al., 2013 and references therein). Recent numerical models and gravity data indeed suggest an efficient coupling between the upper mantle and the crust (e.g., Baratin et al., 2016), which could be triggered by a rollback of the delaminated African lithospheric mantle pulled by a sinking oceanic Western Mediterranean slab (e.g., Bezada et al., 2013; Faccenna et al., 2004). These recent advances in geodesy, seismology, and gravimetry indicate that much of the Rif kinematics cannot be simply associated with the convergence between the Nubia and Iberia plates, but is rather linked to some ongoing delamination and convective removal of the lithospheric mantle beneath the orogen and back-arc opening in the Alboran Sea (Vernant et al., 2010). This complex geodynamic setting yielded shortening in the upper brittle crust approximately along the southern termination of the Rif, as defined by GPS measurements and fault block models (Fadil et al., 2006; Koulali et al., 2011; Vernant et al., 2010).

While geomorphic studies have long demonstrated the tectonic activity of the Rif and the Pre-Rif Ridges (Morel, 1988, 1989), it is only recently that dating techniques such as optically stimulated luminescence or in situ-produced cosmogenic nuclides have enabled determination of time constraints on fault activity in the Rif, such as along the Nekor Fault (Poujol et al., 2014) or the Pre-Rif Ridges (Poujol et al., 2017). The latter have also been identified as a probable source for several historical earthquakes in the Fès-Meknès region (Chalouan et al., 2014; El Mrabet, 2005; Moratti et al., 2003; Poujol et al., 2017) but a reappraisal of the morpho-structures associated with the Pre-Rif front, and their relationships with inherited basement structures, is still needed in order to better characterize their segmentation, kinematics, and seismogenic potential.

This study presents a new set of diagnostic criteria to identify and characterize the tectonic activity of the faults running along the southern Pre-Rif border, taking into account different spatial scales and time windows (Figure 2). Starting from a regional reappraisal of already published data, we provide a new morphochronological data set, using structural morphology and cosmogenic exposure dating (in situ- produced ^{10}Be, ^{26}Al, and ^{36}Cl) of alluvial terraces, bringing additional lines of evidence for tectonic activity along the boundary between the Pre-Rif Ridges and the Saïss Basin (Figure 2). Altogether, this new data set enables us to identify and characterize active structures with slip rates of the order of about 1 mm/yr, providing a basis for a renewed seismic hazard assessment in a region where the large cities of Meknès and Fès host nearly 2 million people.

2. Active Tectonics of Northern Morocco

Although the seismic hazard in Morocco is not as important as in other Mediterranean countries like Italy, Turkey or Greece, it is far from being negligible. Indeed, the relatively superficial nature of the seismicity may combine with weak ground mechanical properties to induce relatively strong accelerations that may lead to significant damage to buildings that do not always meet construction standards (Mourabit et al., 2014). During the last decades, Morocco suffered from several destructive earthquakes such as the Mw 5.9 Agadir event in 1960 or more recently those that struck the region of Al Hoceima in 1994 (M_w 5.7), 2004 (M_w 6.3), and 2016 (M_w 6.3).

In the Gulf of Cadiz, oceanic earthquakes may also be tsunamigenic, like the *Lisbon Earthquake* on November 1, 1755 (M ≈ 8.5–9) (Gutscher, 2004; Gutscher et al., 2006; Johnston, 1996; Martinez-Solares et al., 1979). However, the frequency of such large events remains a major unknown given the uncertainties weighting on the length of the seismic cycle in a context where the tectonic rates are only a few mm/yr (Vernant et al., 2010). In the Gulf of Cadiz, the strongest recent earthquake is that of February 28, 1969 (M_w 7.8; Fukao, 1973). Since 1970, only 19 events have been recorded with a magnitude larger than 5 and only 2 with a magnitude larger than 6 (Matias et al., 2013).

In Morocco, the most seismically active zone is located within the Rif domain (Figure 1). This regional seismicity is mainly distributed within the upper 30 km of crust, although deeper activity is recorded in the eastern part of the Gibraltar Strait, the western Alboran, and in the Middle Atlas (Cherkaoui, 1991; de Vicente et al., 2008; Hatzfeld & Frogneux, 1981; Thiebot & Gutscher, 2006). South of the Rif Mountains, seismicity is significantly more distributed in the Middle Atlas and the High Atlas (Cherkaoui & Asebriy, 2003; Cherkaoui & Medina, 1988; El Alami et al., 1992; Sébrier et al., 2006).

In the majority of cases, historical descriptions of Moroccan earthquakes are not sufficiently detailed to precisely evaluate both the epicentral areas and event intensities. El Mrabet (2005) established a reference list of the main historical earthquakes, compiling and analyzing different catalogs (Cherkaoui & Asebriy, 2003; El Alami et al., 1998; Galbis-Rodriguez, 1932, 1940; Roux, 1934). In close agreement with the distribution of the instrumental seismicity, these historical events are mainly located in the Tell-Rif Alpine chain (Figure 1). Along the southern border of the Rif Mountains, the region of Meknès and Fès has experienced almost 10 earthquakes since the eleventh century (Blanc, 2009; Cherkaoui et al., 2017; El Mrabet, 2005; Mourabit et al., 2014; Peláez et al., 2007; Roux, 1934), with three moderate to large events with intensities ranging between VII and VIII in 1045, 1624, and 1755 (Figure 1). Overshadowed by the large *Lisbon Earthquake* in the historical archives (e.g., Blanc, 2009), the precise date of the *Fès-Meknès Earthquake* is unclear, with Spanish and Portuguese sources referring to a shock on November 18, which could be interpreted as an aftershock of the *Lisbon Earthquake* (Pereira de Sousa, 1919; Roux, 1934; Vogt, 1984), whereas Arab sources document it on November 27, with an epicentral intensity of VIII that was restricted to the Saïss Region (Moratti et al., 2003; Poujol et al., 2017).

3. Material and Methods

3.1. Diagnostic Criteria to Identify and Characterize Moderately Active Faults in Northern Morocco

The search for evidence of fault activity is a long investigation, based on active tectonics, geomorphology, and earthquake geology. Aiming at defining the fault background, it should include not only information on the fault itself but also about its relationships with the seismological and structural environment. Particularly, the fault trace at the surface, as well as its extent, geometry, segmentation, kinematics, and age of activity should be carefully examined together with its relationship with historical and instrumental seismicity.

In this study, we rely on the strategy that was defined in the early 2000s by the international consortium involved in the European Project "Slow Active Faults in Europe" (S.A.F.E.; EVG1-2000-22005), and which aimed at reducing the possible misinterpretations in identifying active faults in the context of slowly deforming regions. The determination of such a set of diagnostic criteria is based on a matrix-like, multi-criteria approach (Figure 2b), which considers that it is key to verify the consistency between the different spatial scales and time windows classically tackled by active tectonic studies. In a simplified manner, the first column of the matrix is interested in the fault existence itself, while the second one is rather focused on the evidence of fault activity at various space scales. The third column deals primarily with the characterization of the fault activity parameters. In a similar way, the first line deals with the regional background of the fault, while the second line mainly concerns fault segmentation, and the third line is interested in more detailed analyses at the site scale (e.g., detailed geomorphic, geophysical studies, or paleoseismic trenches). Logical algorithms were developed by the S.A.F.E. project consortium to address basic questions aimed at a correct diagnosis of fault activity (Siame & Sébrier, 2004). The basic content of each matrix box are documents (maps, tables, geological data...) that may be either available from the literature or from new results obtained during the process. The detailed description of each matrix cell box has been released in a deliverable of the S.A.F.E. project (Siame & Sébrier, 2004).

3.2. Geomorphic Analyses Across Spatial Scales

Once the existence of the tectonic features is established at a regional scale (Figures 3 and 4), the identification and mapping of fault segments generally rely on morphological and structural analyses of satellite images, aerial photographs, digital terrain models, as well as field observations. This makes it possible to map fault systems from a regional scale (≈100 km) to that of the fault segment (≈10 km), and to locate sites deserving more detailed field investigations. In this study, we focused on a morphochronological approach that requires the preservation of tectonically offset landscape features and datable surfaces that can be used to constrain their age (e.g., Ryerson et al., 2006).

To perform a regional survey of the fault system characterizing the front of the Pre-Rif system, a topographical database was built using the Global Digital Surface Model ALOS World 3D (ALOSW3D DSM), with a pixel resolution of 30 m (Takaku et al., 2014, 2018). Ruggedness and topographic position are useful geomorphic tools classically used for landform classification (e.g., Lindsay et al., 2015). To highlight structural and geomorphic features in the studied area (Figure 3), two grids were derived from the ALOSW3D DSM, emphasizing regional topographic gradients: a map of the multiscale elevation residual index (MERI), and a map of the deviation from mean elevation (DEV). These operations were performed using Whitebox Geospatial Analysis Tools (3.4.0. Montreal version release in 2017; Lindsay, 2016). DEV is the difference between the elevation of the spatial window center and its mean elevation, normalized by its standard deviation (Wilson & Gallant, 2000). It is a non-dimensional measure of topographic position scaled by the local ruggedness, which is useful in applications where the landscapes of interest are heterogeneous (De Reu et al., 2013). The MERI also characterizes the topographic position but across a range of spatial scales. The algorithm calculates the difference from mean elevation in a series of window sizes from 3 × 3 to a maximum window size that depends on the size of the DSM. MERI quantifies the proportion of tested scales where the central grid cell has a higher value compared to the mean elevation. Thus, MERI ranges between 0, indicating that a grid cell in a DSM is lower than the mean elevation across the entire range of tested scales, and 1, indicating that the location is consistently higher than the mean elevation (Lindsay, 2016).

To downscale the analysis of the fault morphology at the segment scale (≈10 km), we used data from the Pléiades constellation, composed of two optical Earth-imaging satellites, which provide very-high-resolution images with multi-stereoscopic potential along the same orbit due to their rapid pointing agility (Bernard et al., 2012). In a sparse vegetation setting such as that of the Meknès and Fès region, Pléiades images are a cost-effective alternative to airborne LiDAR to produce high-resolution DSMs of large areas (e.g., Ansberque et al., 2016).

To encompass the fault system running along the southern front of the Pre-Rif Nappe, we specifically acquired 5 Pléiades stereo-couples along a transect centering the fault zone and covering a total area of 3,142 km^2, with a swath width of 20 km (Figure 3). The data set is composed of Pléiades 1B and 1A panchromatic scenes with a resolution of 70 cm, but resampled at a ground sampling distance of 50 cm. The stereoscopic images were then processed to produce a DSM using MicMac photogrammetry open-source software from the French *Institut Géographique National* (Rupnik et al., 2018), and the following workflow pipeline: (1) Satellite images being generated from pushbroom sensors, the geometric model is delivered as Rational Polynomial Coefficients, which is an approximation and needs to be refined; (2) Calculation of the key points on each image with Sift algorithm on sub-sampled images at 5,000 pixels width; (3) The refinement of the orientation is performed with polynomial correction functions estimated from bundle block adjustments of the tie points. Ground control points were not used at this step as none were available, yielding an average residual of about 0.5 pixels (and leading to an elevation uncertainty of about 2 m, e.g., Panagiotakis et al., 2018); (4) The 3-D reconstruction was then done from semi-global multi-view stereo algorithm, pixel to pixel matching from cross-correlation with a moving window of 5 × 5 pixels size. A threshold of 0.2 for minimum correlation was used to avoid low signal/noise ratio. (5) Finally, the resulting DSM was smoothed using a Gaussian filter of 4 × 4 pixels size. The series of Pléiades images as well as the resulting DSM are shown, together with the structural interpretation, in Figure 5.

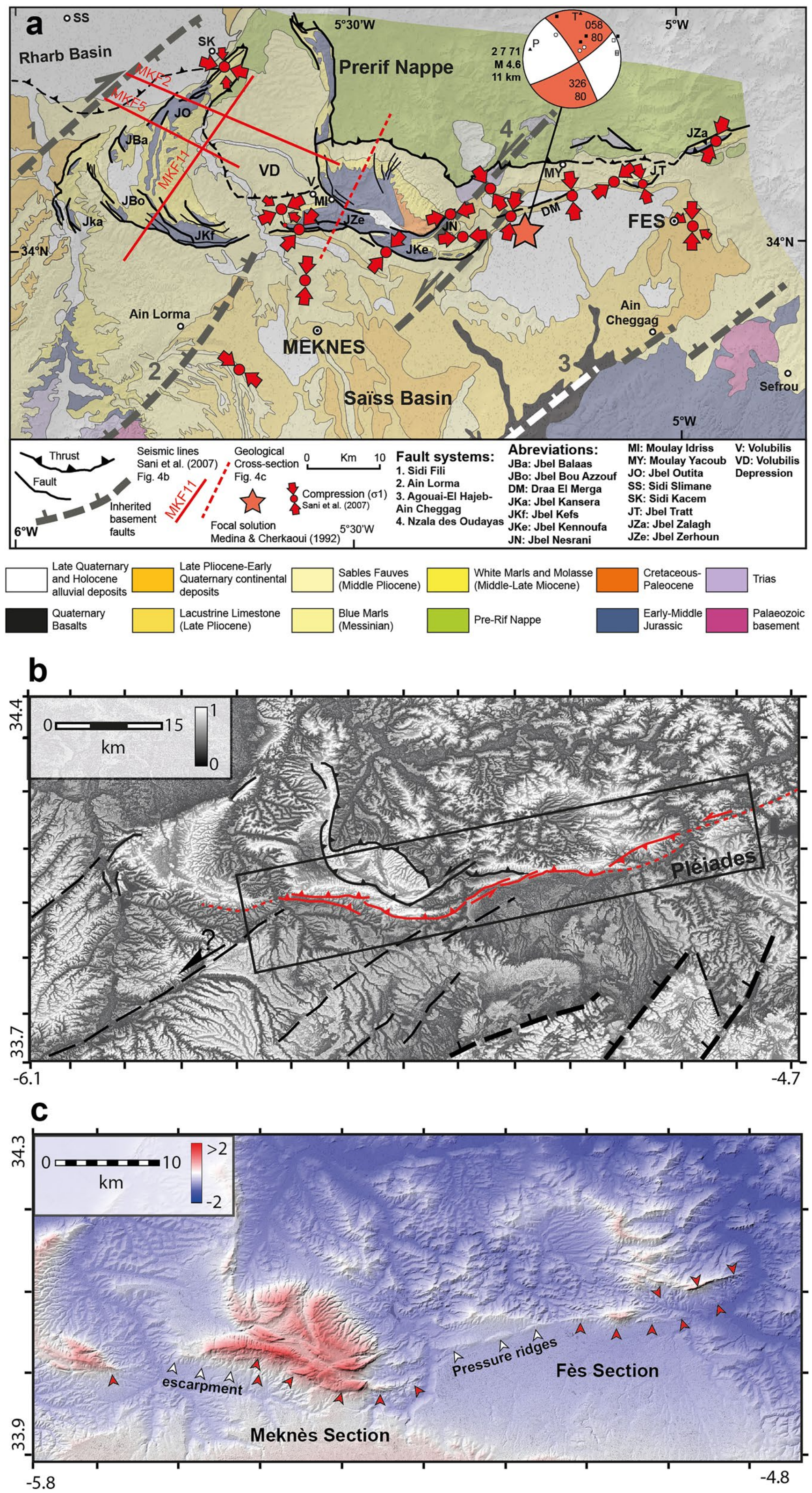
a
SS
Rharb Basin
SK
Prerif Nappe
5°30'W
5°W
2 7 71
M 4.6
11 km
P
T
058
80
326
80
MKF2
MKF5
MKF11
JO
JBa
VD
JBo
Jka
JKf
V
MI
JZe
JN
JKe
DM
MY
JT
JZa
FES
34°N
Ain Lorma
MEKNES
Ain Cheggag
Saïss Basin
Sefrou
1
2
3
4
Thrust
Fault
Inherited basement faults
Seismic lines Sani et al. (2007) Fig. 4b
Geological Cross-section Fig. 4c
Focal solution Medina & Cherkaoui (1992)
Compression (σ1) Sani et al. (2007)
0 Km 10
6°W
Fault systems:
1. Sidi Fili
2. Ain Lorma
3. Agouai-El Hajeb-Ain Cheggag
4. Nzala des Oudayas
Abreviations:
JBa: Jbel Balaas
JBo: Jbel Bou Azzouf
DM: Draa El Merga
JKa: Jbel Kansera
JKf: Jbel Kefs
JKe: Jbel Kennoufa
JN: Jbel Nesrani
MI: Moulay Idriss
MY: Moulay Yacoub
JO: Jbel Outita
SS: Sidi Slimane
SK: Sidi Kacem
JT: Jbel Tratt
JZa: Jbel Zalagh
JZe: Jbel Zerhoun
V: Volubilis
VD: Volubilis Depression
Late Quaternary and Holocene alluvial deposits
Late Pliocene-Early Quaternary continental deposits
Sables Fauves (Middle Pliocene)
White Marls and Molasse (Middle-Late Miocene)
Cretaceous-Paleocene
Trias
Quaternary Basalts
Lacustrine Limestone (Late Pliocene)
Blue Marls (Messinian)
Pre-Rif Nappe
Early-Middle Jurassic
Palaeozoic basement
b
34.4
33.7
-6.1
-4.7
0 15
km
1
0
Pléiades
c
34.3
33.9
-5.8
-4.8
0 10
km
>2
-2
escarpment
Pressure ridges
Fès Section
Meknès Section

10.1029/2020TC006633

3.3. Placing Time Constraints Using Cosmogenic Dating

In this study, in situ-produced ^{10}Be, ^{26}Al, and ^{36}Cl (e.g., Dunai, 2010; Gosse & Phillips, 2001) were used to set temporal constraints for the landscape evolution associated with the tectonic activity. In morphochronology, these cosmogenic nuclides are now routinely used as chronometers to extend the time window of fault slip rate estimates obtained by dating landscape features affected by active tectonics. In dating alluvial landforms using cosmogenic nuclides, surface sampling and/or depth profile approaches are two possible options that can be conducted separately or in combination. However, to successfully date alluvial landforms with profiles, the samples must be collected between the surface and a minimum depth of 5 m (e.g., Braucher et al., 2009; Siame et al., 2012). Otherwise, the cosmogenic concentrations are likely to be dominated by the spallogenic (neutrons) component, which is more sensitive to surface processes than the muonic component at depth. In the studied region, Quaternary alluvial deposits are composed of carbonated clasts and are typically less than 3 m-thick. In such conditions, surface sampling was required. In situ-produced ^{36}Cl concentrations were measured in surface mudstone cobbles and carbonated sandstone cobbles originating from the Jurassic calcareous formations cropping out in the Pre-Rif Ridges and the Miocene Pre-Rif Nappe, respectively (Suter, 1980). In situ-produced ^{10}Be and ^{26}Al concentrations were measured in the quartz isolated from carbonated sandstone cobbles. Prior to chemical procedures, all the samples were crushed and sieved to fractions ranging from 250 and 1,000 μm.

Preparation of in situ-produced ^{36}Cl targets for Accelerator Mass Spectrometry (AMS) measurements consists of 2 h of water-leaching, followed by a 10%-dissolution using HNO_3 (2 $mol.l^{-1}$), and a total dissolution in HNO_3 after addition of 2 mg of a ^{35}Cl-enriched carrier ($^{35}Cl/^{37}Cl = 918$), allowing for simultaneous natural chlorine determination by isotope dilution AMS. For the sandstone cobbles, quartz grains were then recovered from the solution for further ^{10}Be and ^{26}Al procedures. After taking an aliquot for Ca-determination by Inductively Coupled Plasma-Optical Emission Spectrometry, 1 ml of an $AgNO_3$ solution (10%) was added to the dissolved sample to precipitate AgCl. To reduce isobaric interference by ^{36}S during AMS measurements, the AgCl precipitate was re-dissolved using diluted NH_4OH, and sulfur was co-precipitated with $BaCO_3$ to form $BaSO_4$ by addition of an ammoniac saturated $Ba(NO_3)_2$ solution. The solution was filtered (acrodisc 0.45 μm filter) and then AgCl was re-precipitated with diluted HNO_3, washed with water and then dried at 80°C. AMS measurements were performed at the French AMS Facility, ASTER, located at CEREGE in Aix-en-Provence (Arnold et al., 2010). Both the $^{36}Cl/^{35}Cl$ and the $^{35}Cl/^{37}Cl$ ratios were obtained by normalization to an in-house standard (SM-CL-12) with an assigned $^{36}Cl/^{35}Cl$ value of $(1.428 \pm 0.021) \times 10^{-12}$ (Braucher et al., 2018; Merchel et al., 2011), and a natural $^{35}Cl/^{37}Cl$ ratio of 3.217.

For in situ-produced ^{10}Be and ^{26}Al, preparation of targets for AMS measurements followed chemical procedures adapted from Brown et al. (1991) and Merchel and Herpers (1999). Decontamination from atmospheric ^{10}Be of the quartz grains included in the carbonated sandstone cobbles was achieved by a series of three successive leachings in concentrated HF; each leaching removing 10% of the remaining sample mass. Cleaned quartz was then totally digested in concentrated HF, after addition of 100 μg of an in-house carrier at $(3.025 \pm 9) \times 10^{-3}$ g/g of ^{9}Be, originating from a deep-mined phenakite (Merchel et al., 2008). Hydrofluoric and perchloric fuming was used to remove fluorides and both cation and anion exchange chromatography to finally isolate Be and Al. Prior to ^{10}Be and ^{26}Al AMS measurements at ASTER, beryllium and aluminum oxides were mixed to 325-mesh niobium and silver powders, respectively. The ^{10}Be measurements were calibrated against the in-house STD-11 standard ($^{10}Be/^{9}Be = (1.191 \pm 0.013) \times 10^{-11}$; Braucher, 2015). Isotopic $^{26}Al/^{27}Al$ ratios were measured against the in-house standard SM-Al-11, the $^{26}Al/^{27}Al$ value of which $(7.401 \pm 0.064) \times 10^{-12}$ has been cross-calibrated against primary standards from a round-robin exercice (Merchel & Bremser, 2004).

Figure 3. (a) Structural and geological sketch map of the Pre-Rif Ridge at the front of the Pre-Rif Nappe along the northern border of the Saïss Basin (modified after Sani et al., 2007). Red arrows show direction of shortening (after Sani et al., 2007). Solid and dotted red lines locate the seismic lines and geological cross-section depicted in Figures 4b and 4c, respectively. Focal mechanism is after Medina and Cherkaoui (1992). (b) Map of the multiscale elevation residual index (MERI) derived from ALOSW3D DSM. The prominent tectonic features running along the major relief change are depicted in red. Dashed, solid lines indicate possible surface effect of reactivated basement normal faults. The black open rectangle shows the outlay of the Pleiades images used to survey the fault. (c) Map of the deviation from mean elevation (DEV) derived from ALOSW3D DSM. Red arrows indicate prominent geomorphic features running along the major relief change and possibly associated with recent, active tectonic deformation.

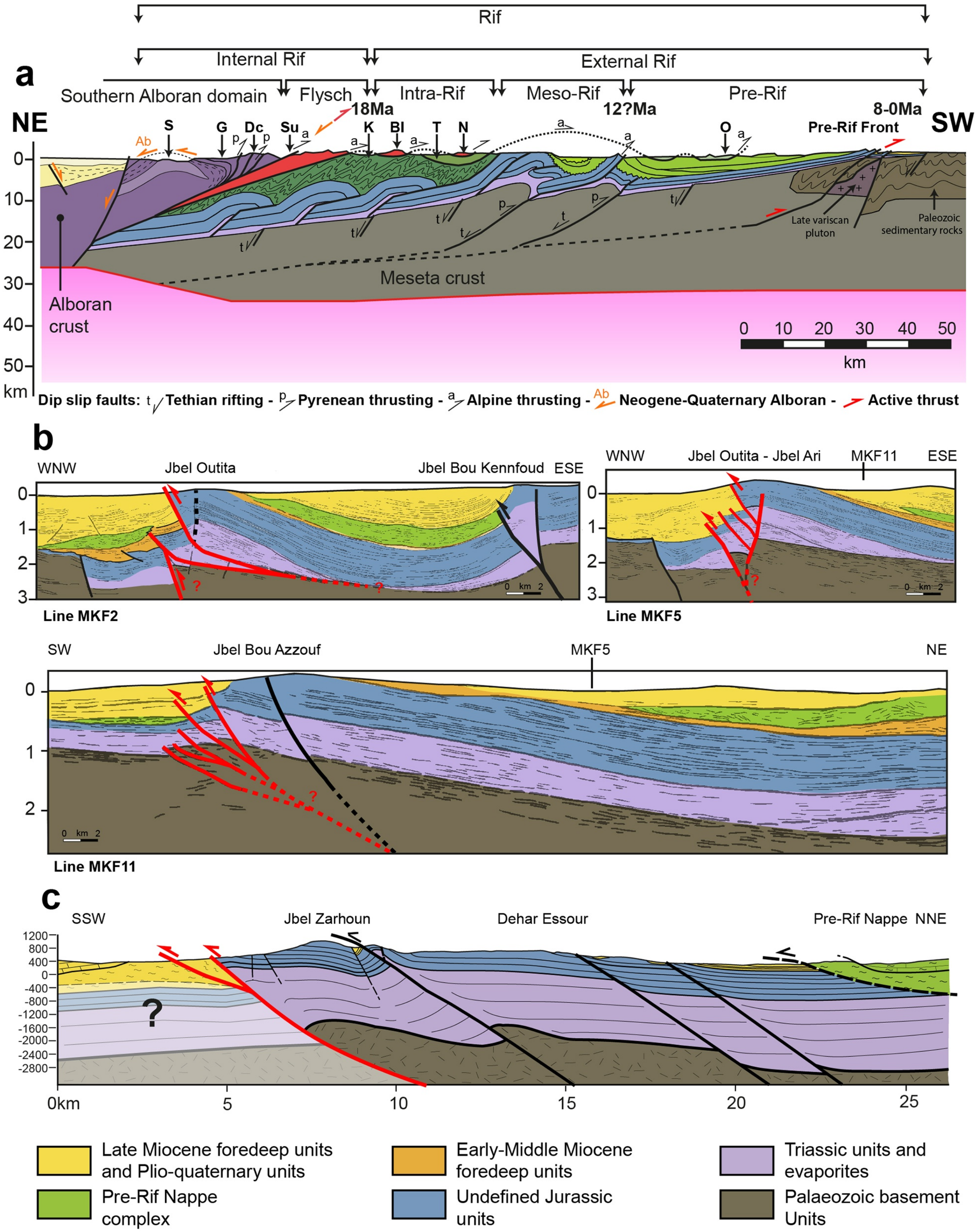
a
Rif
Internal Rif
External Rif
Southern Alboran domain
Flysch
Intra-Rif
Meso-Rif
Pre-Rif
18Ma
12?Ma
8-0Ma
Pre-Rif Front
NE
SW
Meseta crust
Alboran crust
Late variscan pluton
Paleozoic sedimentary rocks
km
Dip slip faults: Tethian rifting - Pyrenean thrusting - Alpine thrusting - Neogene-Quaternary Alboran - Active thrust
b
WNW
Jbel Outita
Jbel Bou Kennfoud
ESE
Line MKF2
Jbel Outita - Jbel Ari
MKF11
Line MKF5
SW
Jbel Bou Azzouf
MKF5
NE
Line MKF11
c
SSW
Jbel Zarhoun
Dehar Essour
Pre-Rif Nappe NNE
0km
Late Miocene foredeep units and Plio-quaternary units
Early-Middle Miocene foredeep units
Triassic units and evaporites
Pre-Rif Nappe complex
Undefined Jurassic units
Palaeozoic basement Units

10.1029/2020TC006633

Reported analytical uncertainties (1σ) include uncertainties in AMS counting statistics, variation of isotopic ratios of standards during the runs, and external AMS uncertainties (Arnold et al., 2010; Braucher et al., 2018). The ^{36}Cl exposure ages were calculated using the Excel® sheet provided by Schimmelpfennig et al. (2009), and a ^{36}Cl sea-level high latitude production rate of 42.2 ± 2.0 atoms ^{36}Cl (g-Ca)/yr (Braucher et al., 2011). Exposure ages from ^{10}Be and ^{26}Al concentrations were calculated using a ^{10}Be sea-level high latitude production rate of 4.01 ± 0.33 atoms ^{10}Be (g-SiO_2)/yr (Borchers et al., 2016), and half-lives of (1.387 ± 0.012) × 10^6 years (Chmeleff et al., 2010; Korschinek et al., 2009) and (0.705 ± 0.024) × 10^6 years (Nishiizumi et al., 2004, 2007), respectively. For all cosmogenic nuclides, exposure ages were calculated using the time-independent scaling functions for high-energy neutrons of Stone (2000), with an attenuation length of 160 g/cm^2, and those of Braucher et al. (2011) for muons. A bulk rock density of 2.5 g/cm^3 was assumed for all samples. With negligible topographic shielding, all minimum exposure ages were calculated with the "zero erosion" assumption (e.g., Lal, 1991).

4. Appraisal of Tectonic Activity Along the Pre-Rif Ridges

4.1. Regional Characteristics of the Pre-Rif Deformation Front

The boundary between the Pre-Rif Ridges and the Saïss Basin has long been investigated through geological (Choubert & Faure-Muret, 1962; Faugères, 1978; Morel, 1988, 1989), structural (Bargach et al., 2004; Frizon de Lamotte et al., 2004; Moratti et al., 2003; Sani et al., 2007), and geodetic (Chalouan et al., 2014; Poujol et al., 2017) approaches. The Pre-Rif Ridges correspond to elongated hills of Mesozoic sedimentary rocks that belong to the Meseta-Atlas cover of the foreland involved in the Late Miocene to Middle Pliocene thrusting of the external Rif (Faugères, 1978; Zizi, 1996).

To the west of the Volubilis Depression (Figure 3), the external Pre-Rif Ridges (Jbel Bou Draa, Outita, Balaas, Kansera, Bou Azzouf, Kefs) form a westward convex, arched-like morphology marking the limit with the Rharb Basin (Bargach et al., 2004), which is probably limited at depth by the NE-striking Sidi Fili fault system (e.g., Sani et al., 2007). To the east of the Volubilis Depression, the internal Pre-Rif Ridges (Jbel Tselfat, Bou Kannfoud, Zerhoun, Kennoufa, Nesrani) form another though wider southward convex, arched-like morphology (Bargach et al., 2004). Further east, along the Pre-Rif deformation front, two insulated ridges (Jbel Tratt and Zalagh) stand on both sides of Fès City (Figure 3).

The ridges are made of a sedimentary sequence that starts with Triassic evaporites and red clays overlain by a relatively thick Jurassic series of dolomite and limestone, and locally by a Marly Cretaceous formation in the eastern ridges (Bargach et al., 2004). The Mesozoic cover is unconformably overlain by Lower and Middle Miocene marls as well as Middle-Upper Miocene sandstones (Figures 3 and 4). From a structural point of view, these deposits generally correspond to SW- and S-verging anticlines associated with the thrusting of the Pre-Rif Nappe, and deforming the Rharb and Saïss Neogene basins, respectively (Figures 3 and 4).

At a regional scale, the morphology associated with the Pre-Rif Ridges is particularly highlighted by the MERI and DEV maps derived from the ALOSW3D digital surface model (Figure 3). The DEV map brings out the major geomorphic features associated with the activity of the faults (fault traces, topographic escarpments, en-échellon pressure ridges...). The MERI map allows mapping the fault geometry and broadly defining the segmentation of the Pre-Rif deformation front into two Meknès and Fès sections. At a first order, this segmentation appears controlled by the interaction between the Pre-Rif thrusts and the NE-striking basement faults below the Mesozoic cover (Figure 3). The Sidi Fili fault system delimits the Khemisset Basin to the northwest (Figures 3 and 4). The Aïn Lorma fault system marks the southeastern shoulder of the Khemisset Basin, and marks the limit between the external and internal Pre-Rif Ridges (e.g., Suter, 1980). According to the seismic lines interpreted by Sani et al. (2007), the Aïn Lorma fault system does not affect

Figure 4. (a) Crustal-scale geological cross-section extracted from TRANSMED-Transect I, depicting the main structures and units between the Alboran Sea and the western Moroccan Meseta (modified after Frizon de Lamotte et al., 2004). Keys: S, Sebtide; G, Ghomaride; Dc, Dorsale calcaire; Su, Suture of the Maghrebian Tethys; K, Ketama Unit; T, Tanger Unit; BI/N, Beni Ider and Numidian nappes; O, Ouezzane Unit. Numbers indicate age of thrusting. (b) Structural interpretation of seismic lines (modified after Sani et al., 2007) with tentative re-interpretation showing active faults marked in red. Vertical scales in two-way time seconds. (c) Schematic geological cross-section of Jbel Zerhoun after the 1/50,000 geological maps of Sidi Kacem (Bendkik et al., 2004) and Beni Ammar (Chenakeb et al., 2004), as well as the stratigraphic logs published in Sani et al. (2007).

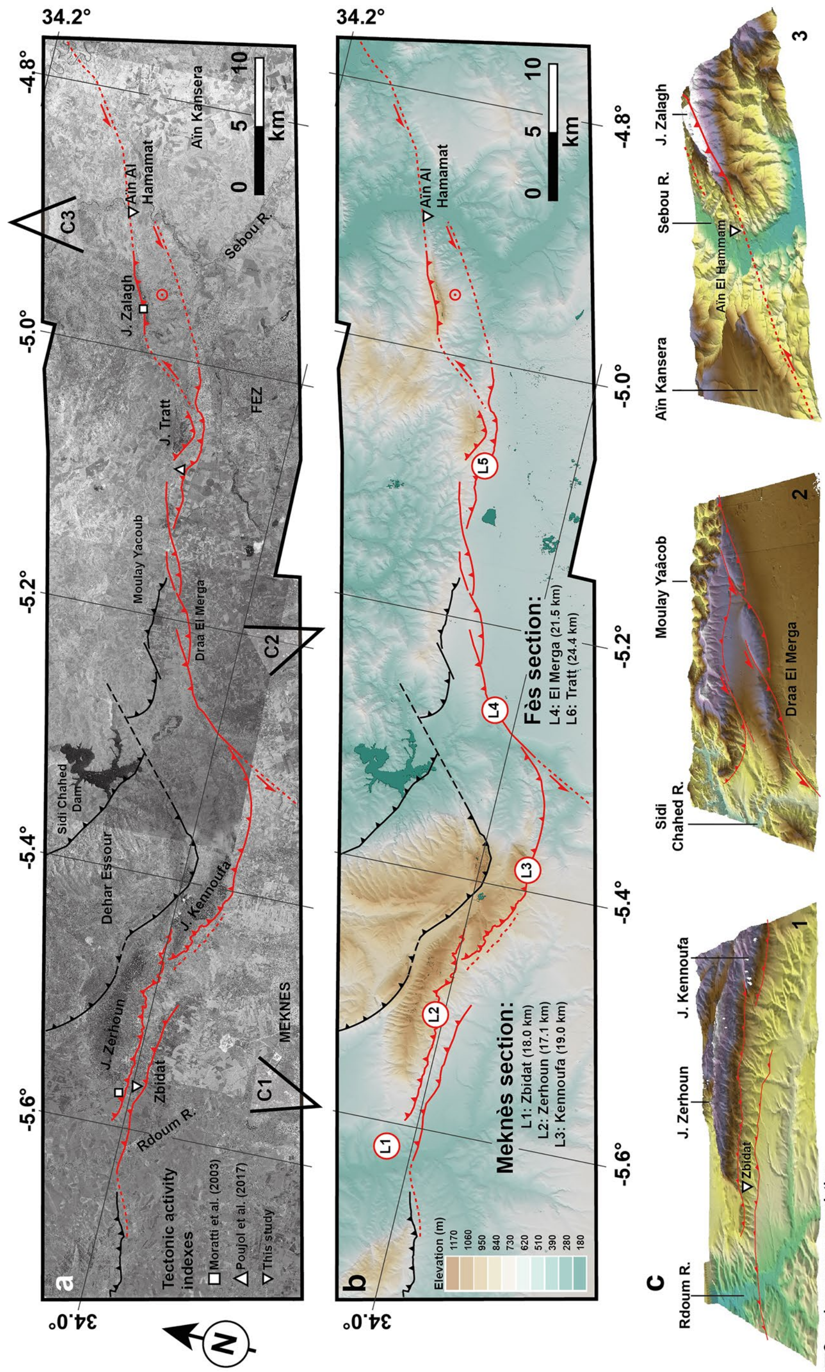

Figure 5. Map of fault traces overlying (a) the mosaic of Pléiades panchromatic scenes specifically acquired in the Fès-Meknès region along the southern Rif deformation front and (b) the digital surface model (DSM) with 1 m pixel resolution derived from stereoscopic pairs, and showing the main fault segments. (c) 3-D bird views extracted from the Pléiades-derived DSM at three specific sites: 1, the Zbidat segment; 2, the El Merga segment; and 3, the termination of the Fès segment, with the Jbel Zalagh pressure ridge. 1 and 2 also locate the sites where the cosmogenic exposure technique has been applied at Zbidat and Aïn Al Hamamat.

the sedimentary deposits overlying the basal part of the Neogene sediment. Nevertheless, the NE-SW linear pattern in the Saïss Basin morphology, evidenced by the MERI map, might well be an evidence of some structural control within the most recent deposits (Figure 3). The Nzala des Oudayas fault system delimits the internal Pre-Rif Ridges to the east of Jbel Kennoufa and Jbel Nesrani, marking the limit between the

Meknès and Fès sections of the fault zone (Figures 3 and 5). This fault system is evidenced by an alignment of Triassic evaporites, and the curvature of the Pre-Rif Nappe front in this area (Figure 3). It also corresponds to the direction of a series of en-échellon pressure ridges, aligned along the Draa El Merga (e.g., Poujol et al., 2017), that are well identified on the DEV map (Figure 3). All these basement faults are clearly imaged on the seismic profiles published by Sani et al. (2007), and characterized by both a sudden increase of the Mesozoic sediment thickness and a basement involvement in the deformation (Figure 4).

Although the Pre-Rif Ridges probably started to develop in the Early Miocene, the most active phase of compression occurred during the Pliocene, with a direction of maximum compression oriented roughly N-S to NE-SW (Figure 3), and a reactivation of the earlier basement, normal faults delimiting the Mesozoic grabens as strike-slip faults (Bargach et al., 2004; Sani et al., 2007). Using GPS measurements and block models (Fadil et al., 2006; Koulali et al., 2011; Vernant et al., 2010), Poujol et al. (2017) estimated that the Pre-Rif front should accommodate a shortening and a left-lateral motion at rates of about 4 and 2 mm/yr, respectively. Chalouan et al. (2014) also suggested that this convergence should be accommodated by ENE-striking, northward-dipping reverse and left-lateral faults, as well as south-verging folds. Along the Pre-Rif front, the only focal mechanism solution available is that of a M 4.6 earthquake, which was recorded on July 2, 1971, close to Moulay Yacoub (Figure 3). Felt with an intensity of V (MSK), the focal solution depicts left-lateral and right-lateral displacements along N326- and N58-striking planes, respectively (Medina & Cherkaoui, 1992). This is exactly the opposite of what would be expected given the geometry of the faults, and the pattern of maximum compression (Figure 3). This contradiction is probably due to the lack of data in the south and west quadrants (Medina & Cherkaoui, 1992). Even if the focal depth of 11 km-deep estimated for this seismic event may be somewhat erroneous, it is worth noting that it is compatible with a slip in the basement and not in the Mesozoic sedimentary cover.

4.2. Segmentation of the Pre-Rif Deformation Front

Geomorphic and structural analyses were carried out along the Pre-Rif Ridges within the region of Meknès and Fès through a detailed mapping of geomorphic markers, using the DSM extracted from the Pléiades stereoscopic scenes and field surveys. Mapping of the geomorphic indicators enabled us to identify and connect several fault segments along the whole fault system, from the westernmost tip of Jbel Zerhoun to Aïn Kansera Plateau to the east (Figure 5). This analysis also permitted us to locate two specific sites of detailed morphochronological investigations (see Section 4.3) at the toe of Jbel Zerhoun, along the Meknès Section, and to the northeast of Fès City, in the pressure-ridge of Jbel Zalagh (Figure 5).

At the toe of Jbel Zerhoun and Jbel Kennoufa, the Pléiades-derived DSM confirms the clear trace of the underlying thrust through the morphology, materialized by two ENE-striking segments of 17 and 18 km-long, respectively (Figure 5). To the west of Jbel Zerhoun, the fault trace is not visible, probably limited at depth by the Aïn Lorma basement fault system. To the east of Jbel Kennoufa, the fault trace runs in the Plio-Quaternary sediments, and curves into a more NE-striking direction, parallel to the structural direction of the Nzala des Oudayas basement fault system (Figure 5).

Beside these two thrust segments, another geomorphic evidence of recent fault activity is a topographic escarpment located to the south of Jbel Zerhoun and north of Rdoum River (Figure 5). In this area, the surface of the Holo-Pleistocene alluvial plain that skirts the toe of the ridge is warped, and exhibits a cumulated topographic escarpment up to 38 m-high (Figure 6). This topographic feature is suggested in the morphology by a series of aligned, renewed gullies generated by backward erosion, strongly suggesting a recent uplift activity (Figure 6). This 14 km-long topographic escarpment can be morphologically traced from the eastern tip of Jbel Zerhoun, although subdued features on the DSM may suggest that it continues up to the eastern tip of the Jbel Kefs, which would extend its length to a maximum of 18 km (Figure 5). Further east, the topographic escarpment fades away, and the DSM does not exhibit clear features beside a few linear traces, limited in length, and without direct connection to the Zbidat escarpment (Figure 5). Based on this morphotectonic analysis, the Pre-Rif front along the Meknès Section can thus be divided into three main reverse segments: Zerhoun (17 km) and Kennoufa (18 km), running at the toe of the carbonated relief, and Zbidat (14–18.5 km), which is marked by the prominent, 38 m-high topographic escarpment warping the more recent alluvial deposits (Figure 5).

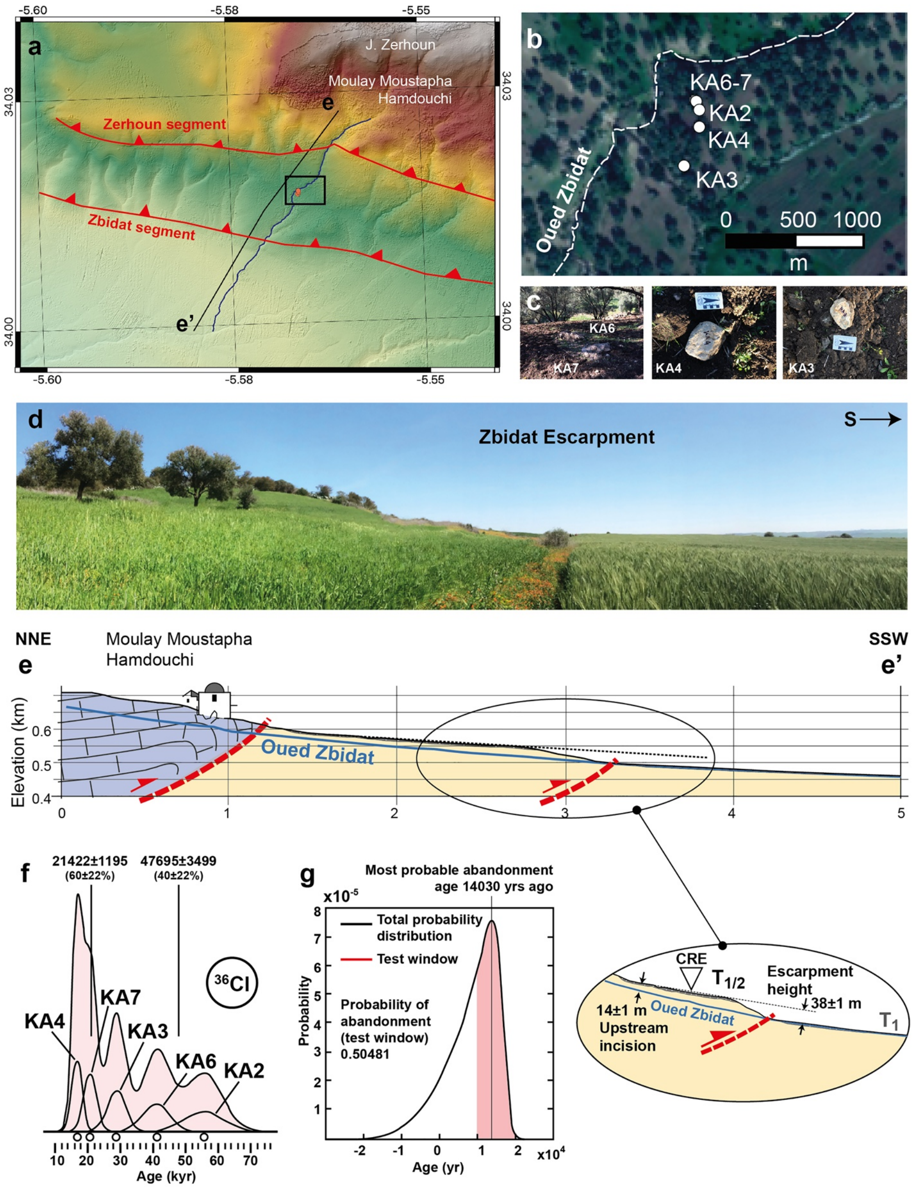

Figure 6. (a) Extract of the Pléiades-derived DSM centered on the Meknès Section and showing the Zbidat escarpment as well as the Zerhoun segment. (b) Localization of the surface samples for cosmic ray exposure dating (Tables 2 and 3). (c) Field photographs of selected samples in their original positions. (d) Field photograph looking eastwardly, showing the topographic escarpment at Zbidat. (e) Topographic cross-section (surface and stream bed) across the escarpment up to the Zerhoun segment, extracted from the Pléiades-derived DSM. The inset shows the upstream incision and escarpment height of 14 ± 1 and 38 ± 1 m, respectively. (f) Cosmogenic exposure dating (^{36}Cl) shown as probability distribution curves and χ^2-test peak ages (Table 4). (g) Probability distribution of abandonment age calculated using the MATLAB tool provided by D'Arcy et al. (2019) over a 11–22 Kyr time window.

To the east of Jbel Kennoufa, the Fès Section is connected to the Meknès Section by the NE-SW trending, ≈22 km-long, El Merga strike-slip segment that parallels the trend of the Nzala des Oudayas basement fault system and connects to a series of aligned, en échellon elongated hills (Figure 5). As already indicated by Poujol et al. (2017), this series of low hills are composed of Plio-Quaternary sediments and associated with laterally offset streams. To the east, this segment connects to the front of the Pre-Rif Nappe, resulting in the maximum 24.4 km-long reverse Tratt segment that runs along the piedmont of the main relief, north of Fès City, to the southern slopes of the Jbel Zalagh. To the east, the subdued fault trace running through the southern hillslopes of Jbel Zalagh does not seem to cross the Sebou River (Figure 5).

Conversely, the northern slopes of the Jbel Zalagh are affected by a clearer, linear, left-lateral and reverse fault trace (e.g., Poujol et al., 2017), suggesting that relief surrounding Jbel Zalagh might well be interpreted as a restraining ridge between the Tratt segment and the continuation of the Pre-Rif front further east (Figure 5). Along the Fès section, the Pre-Rif front is thus mainly composed of the left-lateral El Merga (22 km) and reverse Tratt (24 km) segments, making this portion of the front a zone of relatively more localized deformation than the Meknès Section.

4.3. Temporal Constraints on Geomorphic Evolution at the Site Scale

Along the Meknès and Fès sections (Figure 5), two sites were selected to apply a morphochronological approach using in situ-produced cosmogenic nuclides. In Zbidat, the target morphology corresponds to a Quaternary alluvial surface sitting atop of the 38-m high escarpment running at the toe of the Jbel Zerhoun (Figure 6). Dating the abandonment period of this surface constains the incision rates of the intermittent rivers running across the escarpment, and thus gives a proxy for the local uplift rate associated with the Zbidat segment. In Aïn Al Hamamat, the target morphology corresponds to a series of stepped fluvial terraces that were abandoned by the Sebou River during uplift in the area of the Jbel Zalagh pressure-ridge (Figure 7). Dating the abandonment periods of these fluvial terraces constrains incision rates for the Sebou River, where it crosses the front of the Pre-Rif Nappe, and gives a proxy for the regional uplift rate associated with the deformation front.

In both sites, the geomorphic surfaces are slightly affected by traditional non-mechanical agriculture, with a maximum plowing depth of 30 cm. They are also poor in large, stable surface boulders that are less prone to post-depositional disturbances. Due to this lack of boulders, surface sampling was thus limited to cobbles or large pebbles exceeding 10 cm in diameter. In Zbidat, the surface sampling consisted of three calcareous cobbles and two small boulders that have been chiseled in their topmost part. In Aïn Al Hamamat, the surface sampling consisted of 19 cobbles and pebbles of carbonate or carbonated sandstone (Table 1).

For the two sampled sites, the measured in situ-produced cosmogenic ^{36}Cl concentrations yield a rather well-distributed data set of minimum exposure ages (Tables 2 and 3). In addition, some samples are characterized by a high content in ^{35}Cl (above 100 ppm), which could represent a significant source of uncertainty because of the poorly constrained fluxes of thermal and epithermal neutrons that produce ^{36}Cl through neutron capture (Delunel et al., 2014; Schimmelpfennig et al., 2009). The exposure ages determined for these high ^{35}Cl samples might be overestimated and should be regarded with caution (e.g., Moulin et al., 2016; Rizza et al., 2019). To help improve the interpretation, probability density plots were derived using DensityPlotter, a java application originally designed to interpret populations of single grains from fission track or luminescence dating (Vermeesch, 2012). For each group of cosmogenic exposure ages, a χ^2-test was employed to determine whether their distribution is statistically homogeneous (Table 4). This procedure also determines if the age populations contain more than one mode, yielding in this case mixture age models accounting for both analytical and statistical dispersion (Galbraith & Green, 1990).

For the samples collected on the alluvial surface hanging above the Zbidat escarpment, ^{36}Cl concentrations are ranging from $(0.46 \pm 0.02) \times 10^6$ to $(1.29 \pm 0.07) \times 10^6$ atoms.g^{-1}, with relatively low natural chlorine concentrations (Table 2). These ^{36}Cl concentrations yield minimum exposure ages comprised between 16.8 ± 1.6 and 55.6 ± 5.8 ka (Table 2). For these age population, the probability distribution curve is positively skewed toward older exposure ages (Figure 6), with two principal peaks centered at 21.4 ± 1.2 and 47.7 ± 3.5 ka, and a central value at 29.6 ± 5.8 ka with 43% of dispersion (Table 4).

In Aïn Al Hamamat, measured ^{36}Cl concentrations range from $(0.11 \pm 0.02) \times 10^6$ to $(1.39 \pm 0.07) \times 10^6$ atoms.g^{-1}, yielding minimum cosmogenic exposure ages comprised between 4.4 ± 0.9 and 67.3 ± 7.1 ka (Table 2). For each alluvial surface, a couple of carbonated sandstones also enabled measurements of in situ-produced cosmogenic ^{10}Be and ^{26}Al concentrations (Table 3). In these peculiar samples, ^{10}Be and ^{26}Al concentrations ranged from $(0.17 \pm 0.01) \times 10^6$ to $(0.96 \pm 0.05) \times 10^6$ atoms.g^{-1}, respectively (Table 3). These ^{10}Be and ^{26}Al concentrations yield minimum exposure ages comprised between 35.3 ± 3.2 and 239.1 ± 18.3 ka (Table 3). For the three alluvial surfaces, the age distribution patterns indicate that minimum exposure ages derived from ^{10}Be and ^{26}Al concentrations are generally older than those derived from ^{36}Cl concentrations (Tables 2 and 3).

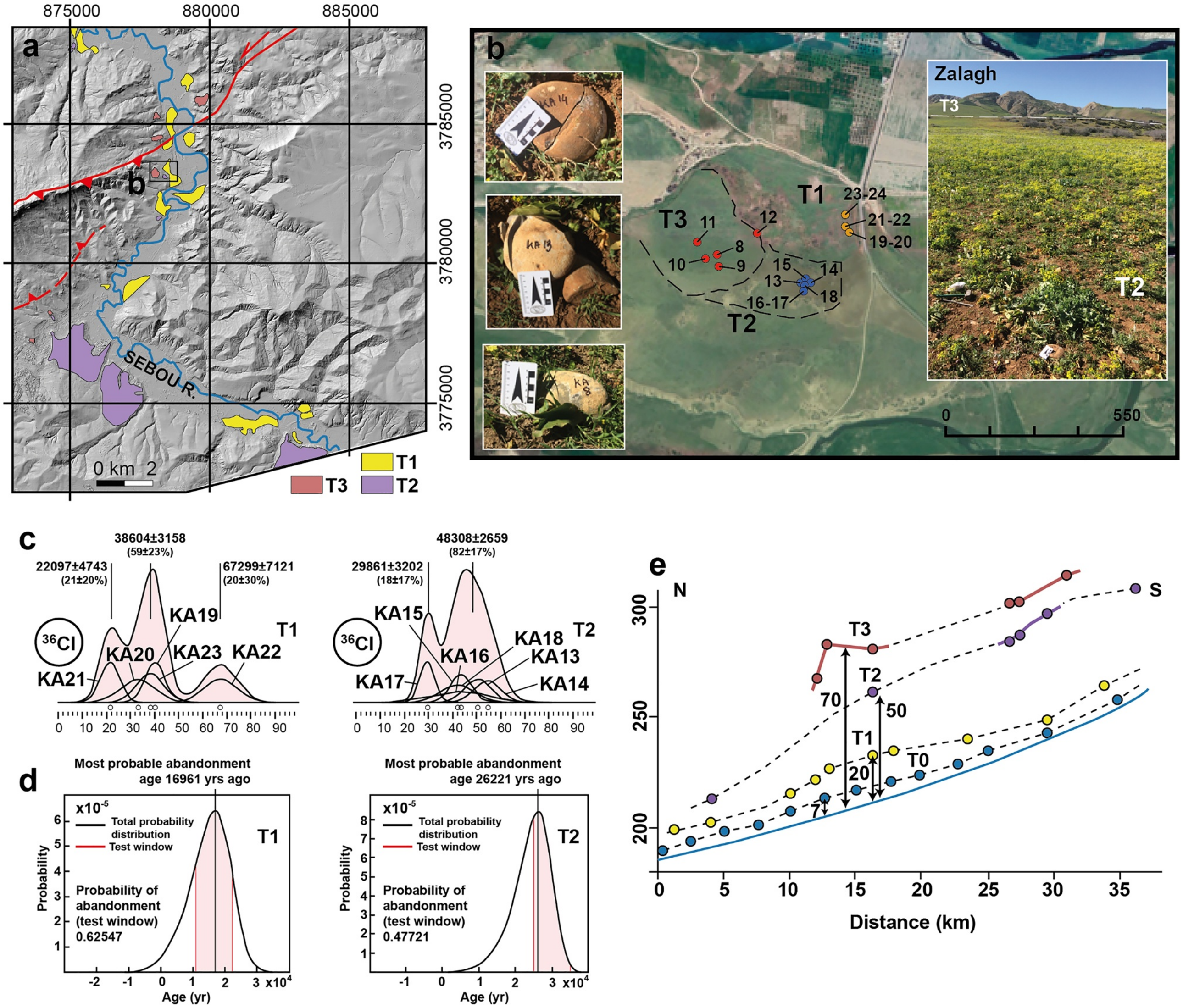

Figure 7. (a) Extract of the Pléiades-derived DSM centered on the Sebou River, east of Fès City, and showing the distribution of the alluvial terraces along the river. (b) Google Earth image extract of Aïn Al Hamamat area showing the position of the samples from the three alluvial surfaces (Tables 1–3). Field photographs show the general morphology of terrace T2 (with T3 in the background) as well as some of the samples in their original position. (c) Cosmogenic exposure dating (^{36}Cl) for T_1 and T_2 shown as probability distribution curves and χ^2-test peak ages (Table 4). (d) Probability distributions of abandonment ages for T_1 and T_2, calculated using the MATLAB tool provided by D'Arcy et al. (2019) over a time window of 11–22 Kyr and 25–35 ka, respectively. (e) Vertical distribution of the alluvial terraces along the Sebou River and estimation of the vertical incision at Aïn Al Hamamat. Elevation points were sampled on the Pléiades-derived DSM.

For the lowest terrace (T_1), the probability distribution of minimum exposure ages derived from ^{36}Cl concentrations is mono-modal (Figure 7), with a central value of 36.7 ± 2.0 ka, which is consistent with the minimum exposure ages derived for one carbonated sandstone (KA19) using ^{10}Be and ^{26}Al concentrations (Tables 2 and 3).

For the middle terrace (T_2), measured ^{36}Cl concentrations yield a majority of the samples agreeing with a minimum exposure age of 48.3 ± 2.7 ka (Figure 7), which is also in relative good agreement with the minimum exposure ages derived for one carbonated sandstone (KA15) using ^{10}Be and ^{26}Al concentrations (Tables 2 and 3). For this population of samples, the χ^2-test also accepts a younger peak at 29.9 ± 3.2 ka, which however relies on only one sample (KA17). Among the samples collected on the middle terrace, two are characterized by high ^{35}Cl contents (KA16 and KA18), and should thus be interpreted with caution.

Table 1
List of Carbonate (Carb.) and Stanstone (Sandst.) Surface Samples for Cosmic Ray Exposure Dating

Sample id	Size/lithology	Location	Geomorphic position	Lat. (WGS84)	Lon. (WGS84)	Elevation (m)	Atm. pressure (mbar)	S.F sp	S.F m	Po ^{10}Be (atoms/g/yr)	Po ^{26}Al (atoms/g/yr)	Po ^{36}Cl (atoms/g/yr)
KA2	Pebble/carb.	Zbidat	T1/T2	34.0143	−5.5661	474	958	1.29	1.24	–	–	24.7 ± 2.1
KA3	Pebble/carb.	Zbidat	T1/T2	34.0140	−5.5662	472	958	1.28	1.24	–	–	27.3 ± 2.3
KA4	Pebble/carb.	Zbidat	T1/T2	34.0142	−5.5661	472	958	1.28	1.24	–	–	28.1 ± 2.3
KA6	Boulder/carb	Zbidat	T1/T2	34.0143	−5.5661	477	957	1.29	1.24	–	–	26.2 ± 2.1
KA7	Boulder/carb	Zbidat	T1/T2	34.0143	−5.5661	477	957	1.28	1.24	–	–	29.5 ± 2.4
KA8	Cobble/carb.	Hamamat	T3	34.1205	−4.9009	279	980	1.10	1.14	–	–	25.9 ± 2.1
KA9	Cobble/carb.	Hamamat	T3	34.1207	−4.9010	279	980	1.10	1.14	–	–	27.8 ± 2.1
KA10	Boulder/sandst.	Hamamat	T3	34.1209	−4.9014	281	980	1.11	1.14	–	–	26.2 ± 2.0
KA11	Cobble/sandst.	Hamamat	T3	34.1214	−4.9017	283	980	1.11	1.14	–	–	26.7 ± 2.1
KA12-3	Pebble/sandst.	Hamamat	T3	34.1216	−4.8997	274	981	1.10	1.13	4.4 ± 0.3	29.2 ± 1.8	38.4 ± 2.8
KA12-4	Pebble/sandst.	Hamamat	T3	34.1216	−4.8997	274	981	1.10	1.13	4.4 ± 0.3	29.2 ± 1.8	27.1 ± 2.1
KA13	Cobble/carb.	Hamamat	T2	34.1202	−4.8980	261	982	1.09	1.13	–	–	23.5 ± 2.0
KA14	Cobble/sandst.	Hamamat	T2	34.1202	−4.8979	261	982	1.09	1.13	4.4 ± 0.3	28.9 ± 1.7	24.1 ± 2.0
KA15	Cobble/sandst.	Hamamat	T2	34.1202	−4.8980	261	982	1.09	1.13	4.4 ± 0.3	28.9 ± 1.7	26.7 ± 2.1
KA16	Cobble/carb.	Hamamat	T2	34.1201	−4.8980	261	982	1.09	1.13	–	–	38.5 ± 2.5
KA17	Cobble/sandst.	Hamamat	T2	34.1201	−4.8980	261	982	1.09	1.13	–	–	25.3 ± 2.0
KA18	Cobble/carb.	Hamamat	T2	34.1202	−4.8980	261	982	1.09	1.13	–	–	27.4 ± 2.1
KA19	Cobble/sandst.	Hamamat	T1	34.1218	−4.8966	233	986	1.06	1.11	4.3 ± 0.3	28.3 ± 1.7	23.7 ± 2.0
KA20	Cobble/carb.	Hamamat	T1	34.1218	−4.8966	233	986	1.06	1.11	–	–	32.6 ± 2.4
KA21	Pebble/carb.	Hamamat	T1	34.1219	−4.8967	233	986	1.06	1.11	–	–	27.8 ± 2.1
KA22	Pebble/sandst.	Hamamat	T1	34.1219	−4.8967	233	986	1.06	1.11	4.3 ± 0.3	28.3 ± 1.7	22.3 ± 1.9
KA23	Cobble/carb.	Hamamat	T1	34.1222	−4.8967	233	986	1.06	1.11	–	–	25.4 ± 2.0

Note. Scaling factors (S.F.) for spallogenic (sp) and muonic (m) contributions are calculated after Stone (2000) and Braucher et al. (2011), respectively.

For the upper terrace (T_3), the measured ^{36}Cl concentrations yield minimum exposure ages that are younger than those obtained for the two other alluvial surfaces (Table 3). This is counter-intuitive since the highest terrace is expected to be the oldest. An alternative interpretation is to consider that this higher alluvial surface has already achieved the cosmogenic steady-state for spallation production pathway (e.g., Lal, 1991). The measured ^{36}Cl concentrations may thus reflect the local denudation rate acting on such alluvial material (Table 2). Besides two samples that are characterized by significantly lower ^{36}Cl concentrations (KA10 and KA11), the others agree on surface lowering rates ranging from 36 ± 3 to 87 ± 12 m/Ma (Table 2). However, most of them are also characterized by high ^{35}Cl contents, and these estimates should thus be considered with caution.

5. Discussion

5.1. Significance of the Cosmogenic Exposure Ages

Conversely to the sandstone coming from the Miocene Pre-Rif Nappe, the carbonate cobbles are derived from more local Jurassic formations that crop out in the Pre-Rif Ridges (Suter, 1980). Indeed, the Sebou watershed is roughly 6,500 km^2 in area upstream of Aïn Al Hamamat, with large fluvial terraces along the river bed (Figure 7). This situation left many opportunities for the sandstone cobbles to experience complex exposure scenarios with alternating burial/exposure episodes during transport. The pair of in situ-produced ^{10}Be and ^{26}Al has long been proposed for studying non-steady eroding horizon (Lal, 1991). For the six carbonated sandstones, the measured ^{26}Al/^{10}Be ratios range from 3.8 ± 0.3 to 5.9 ± 0.5, that is, close to or lower

Table 2
In Situ-Produced ^{36}Cl Concentrations and Associated Minimum Cosmic Ray Exposure Ages at Zbidat and Aïn Al Hamamat

Sample id	Location	Geomorphic position	Mass of dissolved rock (g)	Cl (ppm)	Ca (wt.%)	Mg (wt.%)	^{36}Cl/^{35}Cl ($\times 10^{-13}$)	[^{36}Cl] ($\times 10^{6}$ atoms/g)	Min. ^{36}Cl age (yr)	Max. ^{36}Cl denudation rate (m/Myr)
KA2	Zbidat	T1/T2	65.97	68.7	34.0	0.6	9.10 ± 0.39	1.292 ± 0.067	55,615 ± 5,796	–
KA3	Zbidat	T1/T2	78.76	9.4	54.4	0.0	13.36 ± 0.59	0.759 ± 0.034	28,801 ± 2,843	–
KA4	Zbidat	T1/T2	70.77	21.9	54.1	0.0	5.93 ± 0.26	0.461 ± 0.021	16,758 ± 1,605	–
KA6	Zbidat	T1/T2	72.30	76.1	36.4	0.5	7.02 ± 0.31	1.027 ± 0.058	41,036 ± 4,232	–
KA7	Zbidat	T1/T2	69.73	35.1	55.3	0.0	6.26 ± 0.27	0.597 ± 0.028	20,732 ± 1,978	–
KA8	Hamamat	T3	59.85	55.4	51.7	0.0	3.93 ± 0.18	0.511 ± 0.032	20,236 ± 2,117	77.2 ± 6.7
KA9	Hamamat	T3	58.60	176.4	29.4	0.6	1.72 ± 0.11	0.493 ± 0.058	18,089 ± 2,608	86.6 ± 11.5
KA10	Hamamat	T3	70.41	128.2	35.3	0.5	0.54 ± 0.07	0.114 ± 0.021	4,375 ± 892	363.8 ± 71.6
KA11	Hamamat	T3	72.48	131.4	36.3	0.4	1.02 ± 0.08	0.221 ± 0.029	8,328 ± 1,294	190.3 ± 27.8
KA12-3	Hamamat	T3	27.62	334.3	28.8	0.3	2.75 ± 0.16	1.530 ± 0.177	41,743 ± 6,029	36.5 ± 4.8
KA12-4	Hamamat	T3	41.18	73.8	51.9	0.0	6.01 ± 0.31	1.083 ± 0.066	42,005 ± 4,392	36.3 ± 3.1
KA13	Hamamat	T2	77.06	24.4	51.5	0.0	14.57 ± 0.69	1.125 ± 0.063	50,695 ± 5,458	–
KA14	Hamamat	T2	38.46	33.4	51.3	0.0	9.27 ± 0.40	1.243 ± 0.059	54,892 ± 5,612	–
KA15	Hamamat	T2	27.33	78.4	50.6	0.0	4.81 ± 0.25	1.101 ± 0.062	43,653 ± 4,399	–
KA16	Hamamat	T2	61.03	345.7	28.6	0.6	3.19 ± 0.18	1.603 ± 0.361	43,653 ± 10,877	–
KA17	Hamamat	T2	56.98	53.8	51.3	0.0	5.54 ± 0.26	0.724 ± 0.042	29,583 ± 3,056	–
KA18	Hamamat	T2	62.98	181.7	28.6	0.6	3.82 ± 0.20	1.105 ± 0.150	42,175 ± 6,911	–
KA19	Hamamat	T1	18.04	39.4	50.2	0.0	3.70 ± 0.19	0.908 ± 0.048	40,154 ± 4,155	–
KA20	Hamamat	T1	62.03	268.5	28.3	0.6	2.60 ± 0.15	1.042 ± 0.206	33,205 ± 7,306	–
KA21	Hamamat	T1	64.19	197.1	28.4	0.6	1.91 ± 0.12	0.586 ± 0.101	21,559 ± 4,180	–
KA22	Hamamat	T1	34.15	33.3	46.9	0.1	9.56 ± 0.42	1.392 ± 0.065	67,329 ± 7 100	-
KA23	Hamamat	T1	62.98	158.9	28.8	0.6	3.59 ± 0.19	0.933 ± 0.111	38,316 ± 5,725	–

Note. Samples KA2 to KA7 were processed together with a blank sample yielding a ^{36}Cl/^{35}Cl ratio of $(3.63 \pm 0.94) \times 10^{-15}$. The others were processed with another blank sample yielding a ^{36}Cl/^{35}Cl ratio of $(2.65 \pm 0.89) \times 10^{-15}$.

than the theoretical surface steady-state value of 6.1 ± 0.5 (Stone, 2000). The low ^{26}Al/^{10}Be ratios can be interpreted as reflecting temporary burial of the material (Granger & Muzikar, 2001) or regolith mixing in a slowly eroding landscape (Makhubela et al., 2019).

For the carbonate samples, the dispersion of minimum ^{36}Cl exposure suggests that (1) the older samples might also carry cosmogenic content inherited from pre-exposure in the upstream areas, and (2) natural post-abandonment processes (i.e., water runoff, surface deflation) might have, combined with human activities, resulted in upward displacement of cobbles that were initially buried within the first half-meter of alluvial material. This later case could explain the younger ages in the distributions. An alternative interpretation is to consider that the age dispersion is actually representative of the time span of surface activity before abandonment and consequent to an incision of the drainage network. (e.g., Owen et al., 2011). In this scenario, the average value of the age population would fall during the true time span of surface deposition, with the maximum and the minimum ages approximating the beginning of surface activity and the timing of surface abandonment, respectively (D'Arcy et al., 2019).

In Zbidat, the central value of 29.6 ± 5.8 ka is only a rough estimate of the abandonment period of the surface. Assuming that the surface abandonment coincided with an abrupt landscape uplift due to the fault activity, the probabilistic approach developed by D'Arcy et al. (2019) considers that this event should be recorded by the age of the youngest sample, depending on the overall period of surface activity. Assuming that the older carbonate cobble is an outlier carrying cosmogenic inheritance, the dispersion of the remaining minimum exposure ages can thus be interpreted as the result of a 41 Kyr time-span of surface activity,

Table 3
In Situ-Produced ^{10}Be and ^{26}Al Concentrations and Associated Minimum Cosmic Ray Exposure Ages at Aïn Al Hamamat

Sample id	Mass of quartz (g)	Mass of spike ^{9}Be (g)[a]	$^{26}Al/^{27}Al$ ($\times 10^{-13}$)	[^{26}Al] ($\times 10^{6}$ atoms/g)	Min. ^{26}Al age (yr)	$^{10}Be/^{9}Be$ ($\times 10^{-13}$)	[^{10}Be] ($\times 10^{6}$ atoms/g)	Min. ^{10}Be age (yr)	$^{26}Al/^{10}Be$
KA12-3/T3	27.19	0.1511	15.05 ± 0.5	4.098 ± 0.144	150,732 ± 10,483	6.24 ± 0.25	0.698 ± 0.029	164,407 ± 11,950	5.9 ± 0.3
KA12-4/T3	20.07	0.1523	2.05 ± 0.15	1.488 ± 0.111	52,183 ± 4,987	2.61 ± 0.11	0.396 ± 0.017	91,574 ± 6,725	3.8 ± 0.3
KA14/T2	13.34	0.1519	8.53 ± 0.47	1.872 ± 0.100	66,829 ± 5,358	1.60 ± 0.08	0.362 ± 0.018	84,473 ± 6,604	5.2 ± 0.4
KA15/T2	26.55	0.1539	3.75 ± 0.22	1.080 ± 0.063	38,012 ± 3,189	1.63 ± 0.07	0.188 ± 0.008	43,481 ± 3,200	5.7 ± 0.4
KA19/T1	26.12	0.1525	3.25 ± 0.22	0.982 ± 0.066	35,337 ± 3,178	1.43 ± 0.07	0.166 ± 0.009	39,186 ± 3,111	5.9 ± 0.5
KA22/T1	7.22	0.1530	5.92 ± 0.30	4.333 ± 0.224	166,103 ± 13,146	2.29 ± 0.11	0.964 ± 0.046	239,061 ± 18,300	4.5 ± 0.3
Blank	–	0.1530	$<2.76 \times 10^{-15}$	–	–	$(2.37 \pm 0.32) \times 10^{-15}$	–	–	–

Note. Exposure ages are calculated neglecting muonic contribution at the surface as it accounts for less than 3% of the total production. ^{10}Be and ^{26}Al were performed at ASTER AMS facility. BeO machine blank $^{10}Be/^{9}Be$ ratio is 3.55×10^{-16}. Al_2O_3 machine blank $^{26}Al/^{27}Al$ ratio is 2.95×10^{-15}.
[a]In-house carrier at $(3.025 \pm 9) \times 10^{-3}$ g/g of ^{9}Be; No ^{27}Al spike was added.

with a 50% chance of an abandonment time falling between 11 and 22 ka (Figure 6). In this scenario, the period of surface activity can thus be bracketed between the older peak at 47.7 ± 3.5 ka and the younger peak at 21.4 ± 2.0 ka (Table 4). At Aïn Al Hamamat, considering the older age as an outlier due to cosmogenic inheritance, the lower surface (T_1) may have experienced a 31 Kyr time-span of surface activity, with a 63% chance of an abandonment time falling between 11 and 22 Kyr (Figure 7). In this scenario, the lower terrace at Aïn Al Hamamat can be regarded as contemporaneous with the alluvial surface that skirts the piemont of Jbel Zerhoun along the Meknès Section. As for the middle surface (T_2), it may have experienced a 35 Kyr time-span of surface activity, with a 48% chance of an abandonment time falling between 25 and 35 Kyr (Figure 7).

5.2. Estimation of Pleistocene Rates of Displacement

At Zbidat, the 38 m-high topographic escarpment represents the vertical cumulative displacement generated by a 18 km-long reverse fault segment (Figure 5). Along the trace of this segment, temporary streams have cut through the topography, creating 14 m-deep upstream incisions (Figure 6). Since there is no temporal constraint on the age of the surface laying at the toe of the escarpment, the height of the escarpment should be regarded as a minimum value for the vertical displacement. Assuming that uplift started as early as the onset of surface activity (i.e., 47.7 ± 3.5 ka), a minimum vertical rate of 0.8 ± 0.1 mm/yr can be estimated. This assumption is consistent with that of considering an abandonment of the alluvial surface (i.e., 21.4 ± 2.0 ka), which coincides with the onset of the stream incision and yields an incision rate of 0.7 ± 0.1 mm/yr. However, given the uncertainties associated with the dating of the surface abandonment, a wider bracketing of the incision rate between 0.6 and 2.0 mm/yr cannot be ruled out.

At Aïn Al Hamamat, the profiles of the stepped terraces exhibit a convincing warping where the Sebou River crosses the front of the Pre-Rif Nappe (Figure 7). At the latitude of the Jbel Zalagh pressure ridge, the lower,

Table 4
Statistical χ^2-Tests Performed Using DensityPlotter (Vermeesch, 2012) and Most Probable Abandonment Ages Using the Probabilistic Approach of D'Arcy et al. (2019)

Group of samples	Geomorphic position	Number of samples	Central value years (1σ)	Dispersion	$P(\chi^2)$	Peak 1 years (1σ)	Peak 2 years (1σ)
Zbidat	T1/T2	5	29,582 ± 5,780	0.43	0.00	21,423 ± 1,195 (60%)	47,695 ± 3,499 (40%)
Hamamat	T2	6	43,338 ± 3,976	0.18	0.00	29,861 ± 3,202 (18%)	48,308 ± 2,659 (82%)
Hamamat	T1	4	33,751 ± 3,898	0.17	0.04	22,098 ± 4,744 (26%)	38,602 ± 3,157 (74%)

middle and higher terraces lie at elevations of 20 ± 2, 50 ± 2, and 70 ± 2 m-high above the present-day river bed (Figure 7). In the same area, the Sebou River is also more entrenched into its major flood plain, with an incision of about 7 ± 2 m (Figure 7). On the one hand, based on the abandonment of the lower and middle terraces at 22.1 ± 4.7 and 29.9 ± 3.2 ka, the topographic positions of these two features above the present-day river bed imply vertical incision rates of the Sebou River of the order of 1.0 ± 0.3 and 1.7 ± 0.2 mm/yr. On the other hand, accounting for the entire periods of surface activity, estimated by the central values of 38.6 ± 3.1 ka (T1) and 48.3 ± 2.7 ka (T2), yields lower vertical rates of 0.5 ± 0.1 and 1.0 ± 0.1 mm/yr, respectively. Standing at about 7 ± 2 m above the Sebou River, the major flood plain (T0) is not dated but it is certainly younger than the lower terrace. Assuming a Holocene (11 ± 1 ka) onset for this late river incision yields a rate of about 0.7 ± 0.3 mm/yr, which is consistent with previous lower bound estimates. Since the Sebou River is a major regional drainage system, and without trying to account for transient changes in the watershed during the uplift, one can thus consider that a mean incision rate of 0.9 ± 0.2 mm/yr is a reasonable proxy for the last 50 ka. This value is comparable to the lower bound estimated at Zbidat along the Meknès Section (0.7 ± 0.1 mm/yr). However, if one agrees that tectonic uplift is fully responsible for the stepped geometry of the alluvial terraces along the Sebou River, the roughly 30 m-elevation difference between T1 and T2 should have occurred after the onset of activity of T2 (48.3 ± 2.7 ka) and before that of T1 (38.6 ± 3.1 ka), implying a vertical uplift rate higher than 2 mm/yr over a short time span. Finally, due to the relatively large uncertainties associated with individual samples and the resulting distributed age populations, it is rather speculative to go further on this. In the following, we will thus consider that a value comprised between 0.6 and 2 mm/yr is a conservative proxy for uplift rates associated with the tectonic activity of the faults running along the Pre-Rif Ridges.

In the Rif region, geological markers such as the post-nappe surface (Late Tortonian, 7.3 Ma) and the summit surface of the Pre-Rif Nappe (Messinian, 5.3 Ma, to Pliocene, 2.6 Ma) are classically used to gauge long-term neotectonics (Carte Néotectonique du Maroc, 1994; Morel, 1988, 1989). Along the deformation front running at the border of the Saïss Basin, these markers exhibit vertical steps ranging from 1,600 to 1,800 m (Carte Néotectonique du Maroc, 1994), implying long-term, vertical rates of the order of 0.5 ± 0.2 mm/yr. The lower bound of our Pleistocene rate is thus consistent with this integration over the last several millions of years.

At the toe of Jbel Tratt in the middle of the Fès Section (Figure 5), Poujol et al. (2017) described a minimum 12 ± 1 m-high, vertical displacement for an alluvial surface with an optically stimulated luminescence age ranging from 5.2 ± 0.2 ka (minimum burial age) to 8.1 ± 0.9 ka (central age model). This local observation implies an uplift rate comprised between 1.5 ± 0.3 and 2.3 ± 0.3 mm/yr, which is also consistent with the upper bound of our Pleistocene rate estimate.

5.3. Seismic Hazard Parameters

In terms of seismogenic potential, the rooting of the Pre-Rif faults at depth is an important parameter to consider. According to published regional cross-sections, the southern deformation front of the external Rif domain could either sole in the Trias at the base of the Mesozoic cover above the African basement at about 3–5 km-depth (Michard et al., 2002, 2008) or into the African lower crust at about 25 km-depth (Frizon de Lamotte et al., 2004). Existing seismic lines along the Fès and Meknès sections, as well as in the external Pre-Rif Ridges (Sani et al., 2007; Zizi, 1996), also favor a rooting in the basement of the Miocene thrusts, reactivating former Mesozoic normal faults (thick-skinned option 2, Figure 8) rather than within the Trias at about 3–5 km-depth (thin-skinned option 1, Figure 8). This is also consistent with a focal depth of about 10 km for the 1971 M_w 4.6 earthquake, close to Moulay Yacoub (Medina & Cherkaoui, 1992), which could be associated with either the Nzala des Oudayas basement fault or the Pre-Rif front (Figure 3).

On the seismic lines interpreted by Sani et al. (2007), the faults associated with the post-Tortonian uplift of the Pre-Rif Ridges appear relatively steep and rooted in the basement (Figure 4b), even if they might be shallower toward the surface in other locations (Figures 4c and 6e). For the Pre-Rif Ridges a listric geometry has also been considered at greater depth (Chalouan et al., 2001; Poujol et al., 2017). Without additional geometrical constraints, we can assume that the Pre-Rif thrusts are characterized by fault planes dipping between 30° and 60° at depth. Along the Meknès and the Fès sections, the length of the segments are of the order of 17–24 km (Figure 5). According to scaling relationships (e.g., Thingbaijam et al., 2017; Wells

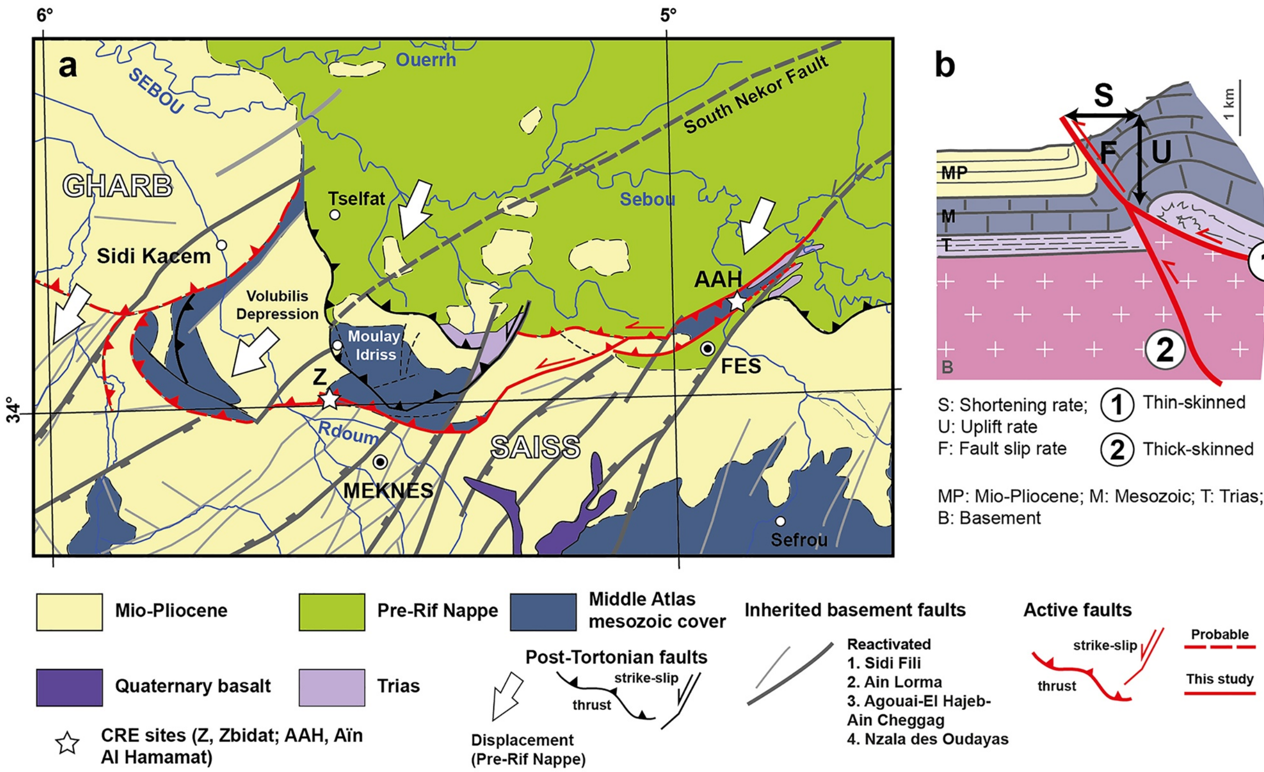

Figure 8. (a) Structural framework showing the relationship between inherited basement normal faults (after the Carte Néotectonique du Maroc, 1994) and surface expression of active faults along the front of the Pre-Rif Nappe. (b) Sketch of the main frontal thrust, showing the two rooting possibilities at depth: (1) a thin-skinned option where the reverse fault sole at about 3–5 km-depth in the Trias, dipping at 30°; (2) a thick-skinned option where the reverse fault connects to inherited basement faults, dipping at 60°. Arrows indicate uplift rate (U, 0.6–2.0 mm/yr), estimated from measured incision values and cosmogenic surface dating, fault slip rate (F, 0.7–4.0 mm/yr) and shortening rate (S, 0.4–3.5 mm/yr), estimated using a fault dip ranging from 30° to 60°.

& Coppersmith, 1994), this range of surface lengths for reverse faults generally correspond to maximum moment magnitudes of about 6.4–6.8 (Table 5). These magnitude estimates are compatible with intensities ranging between VII and VIII for moderate to large historical earthquakes reported for this region since the eleventh century, and particularly with that of the 1755 *Fès-Meknès Earthquake* (Blanc, 2009; Cherkaoui et al., 2017; El Mrabet, 2005; Peláez et al., 2007; Mourabit et al., 2014; Roux, 1934). Since scaling laws are statistically consistent with self-similarity (e.g., Thingbaijam et al., 2017), relationships between rupture

Table 5
Seismic Hazard Parameters Form Empirical Earthquake Scaling Laws From Thingbaijam et al. (2017) and Hanks and Kanamori (1979)

Segment name	Label of Figure 5	Sens of motion	Length (km)	Rupture area (km^2) 30° or 60°	M_w	Average displacement (m)	Return time (yr)
Zbidat	L_1	Reverse	18	254	6.5 ± 0.1	0.6	150–850
Zerhoun	L_2	Reverse	17	240	6.4 ± 0.1	0.5	140–790
Kennoufa	L_3	Reverse	19	268	6.5 ± 0.1	0.6	160–920
El Merga	L_4	Left-lateral	22	311–339	6.3 ± 0.1	0.3	90–500
Tratt	L5	Reverse	24	339	6.6 ± 0.1	0.9	220–1290
Meknès	$L_2 + L_3$	Reverse	35	–	6.7 ± 0.1	–	–
Fès	$L_4 + L_5$	Reverse/LL	46	–	7.8 ± 0.2	–	–
All		Reverse	82	–	7.1 ± 0.1	–	–

Note. Return times are estimated using a fault slip rate ranging from 0.7 and 4.0 mm/yr.

area versus M_w, and rupture length versus M_w offer the opportunity to explore the characteristic seismogenic depth beneath the Pre-Rif Ridges (Table 5). To be consistent with fault dipping between 30° and 60° at depth (Figure 8), and with the moment magnitudes deduced from segment lengths, the seismogenic depth of the faults should be of the order of 7–12 km (Table 5).

Finally, combining measured segment lengths, with estimated seismogenic depths and M_w from scaling relationships on the basis of formulations by Aki (1964) and Hanks and Kanamori (1979) yields average coseismic displacements of the order of 0.4–0.9 m (Table 5).

Our projection of an uplift rate of 0.6–2.0 mm/yr onto a 30° to 60°-dipping fault plane (Figure 8), would result in conversions to fault slip rates ranging from 0.7 to 4 mm/yr, and shortening rates of 0.4–3.5 mm/yr (Figure 8). Even if the fault slip rate is clouded by large uncertainties, such coseismic displacements imply recurrence intervals on the order of a several centuries (Table 5), in good agreement with the historical catalog that describes several M ≈ 6 events since 1045 CE (El Mrabet, 2005). The bracketing of horizontal shortening is also consistent with that derived by Poujol et al. (2017) and with what is expected from the horizontal GPS velocities and fault block models (e.g., Fadil et al., 2006; Koulali et al., 2011; Vernant et al., 2010). This consistency between the geodetic and geomorphic time scales strongly confirms that the southern border of the Pre-Rif is an important tectonic boundary (e.g., Poujol et al., 2017; Vernant et al., 2010) that probably accommodated most of the shortening associated with the lateral extrusion of the Rif during the Pleistocene.

6. Conclusions

In this study, we revised the regional geomorphic characteristics of the faults running along the front of the Pre-Rif Ridges that constitute the southern border of the Alpine Rif domain in Morocco. Along the ≈80 km-long left-lateral, transpressive and reverse fault zone, we provide new geomorphic lines of evidence supporting the Quaternary activity on fault segments that are characterized by lengths of about 20 km. The fault zone can be divided into the Meknès and the Fès sections, which are most probably limited at depth by reactivated, NE-trending basement faults that delineate paleo-grabens associated with the Late Triassic-Jurassic opening of the Atlantic Ocean.

Although the chronological data set provided by cosmogenic nuclides is not straightforward to interpret, the morphochronological approach applied to date stepped alluvial surfaces above the present-day drainage network, allows estimation of incision rates in the range of 0.6–2.0 mm/yr, which can be interpreted as a reasonable proxy for the uplift rate associated with the front of the Pre-Rif Nappe during the last 50 ka.

Given their characteristic lengths of about 20 km, the identified fault segments should root in the basement at about 7–12 km-depth, and would have the capacity to generate earthquakes with moment magnitudes of 6.3–6.8, average displacements of a few tens of centimeters, and return periods of the order of several hundreds of years. A comparison of different time scales suggests that the fault slip rate associated with the front of the Pre-Rif Nappe has been relatively constant over the last few millions of years, even if a degree of recent acceleration cannot be excluded. Altogether, the results presented in this study imply that the front of the Pre-Rif Nappe is an important structural boundary that may have accommodated most of the Rif lateral extrusion between the Nubia and Iberia tectonic plates.

Data Availability Statement

Data sets for this research are available in this in-text data citation references: Agharroud et al. (2021) [Creative Commons Attribution 4.0 International]. The AW3D30 (version 3.1) topographic data used for this paper is provided by the Japan Aerospace Exploration Agency.

Acknowledgments
During the revision process, Didier Bourlès sadly passed away. Didier was a renowned scientist who contributed significantly to the development of the technique of cosmogenic nuclides, rendering it essential to many applications in geosciences. We would like to dedicate this article to his memory. This work has been funded by the RiskMED project, Labex OT-Med (ANR-11-LABE-0061) supported by the Investissements d'Avenir, French Government project of the French Agence National pour la Recherche (ANR) through the A*MIDEX project (ANR-1-1E-0001-02). The Pléiades images used in this study were specifically acquired through an ISIS Project funded by the CNES (FC-193978-2018-311-U. AIX-Marseille CEREGE). The ASTER AMS national facility (CEREGE, Aix-en-Provence), where the ^{10}Be, ^{26}Al, and ^{36}Cl measurements were carried out, is supported by the INSU/CNRS, the ANR through the Projets thématiques d'excellence programme for the Equipements d'Excellence ASTER-CEREGE action, and the IRD. We thank Georges Aumaître and Karim Keddadouche for their continuing expertise in Accelerator Mass Spectrometry measurements. We thank Régis Braucher and Lucilla Benedetti, from CEREGE, as well as Philippe Vernant, from Montpellier University, and Jason Williams, from Leeds University, for thoughtful reviews of an early version of this paper. We thank both Timothy Byrne, from University of Connecticut, and Edward Anthony, from Aix-Marseille University, for editing the English. Figure 1 was created using the GMT software package. Taylor Schildgen and Duna Roda-Boluda are thanked for their editorial handling of the manuscript.

References

Abbassi, A., Cipollari, P., Zaghloul, M. N., & Cosentino, D. (2020). The Rif Chain (Northern Morocco) in the Late Tortonian-Early Messinian Tectonics of the Western Mediterranean orogenic belt: Evidence from the Tanger-Al Manzla wedge-top basin. *Tectonics*, *39*(9), e2020TC006164. https://doi.org/10.1029/2020TC006164

Agharroud, K., Siame, L., Ben Moussa, A., Bellier, O., Guillou, V., Fleury, J., & El Kharim, Y. (2021). *AMS results for cosmogenic exposure dating along the Southern Rif Front of Morocco (Version 1.0) [Data set]*. Zenodo. https://doi.org/10.5281/zenodo.4543677

Aki, K. (1966). Generation and propagation of G Waves from the Niigata Earthquake of June 16, 1964: Part 1. A statistical analysis. 東京大學地震研究所彙報= *Bulletin of the Earthquake Research Institute*, *44*, 23–72.

Ansberque, C., Bellier, O., Godard, V., Lasserre, C., Wang, M., Braucher, R., et al. (2016). The Longriqu fault zone, eastern Tibetan Plateau: Segmentation and Holocene behavior. *Tectonics*, *35*(3), 565–585. https://doi.org/10.1002/2015TC004070

Arnold, M., Merchel, S., Bourlès, D. L., Braucher, R., Benedetti, L., Finkel, R. C., et al. (2010). The French accelerator mass spectrometry facility ASTER: Improved performance and developments. *Nuclear Instruments and Methods in Physics Research Section B: Beam Interactions with Materials and Atoms*, *268*(11–12), 1954–1959.

Baratin, L. M., Mazzotti, S., Chéry, J., Vernant, P., Tahayt, A., & Mourabit, T. (2016). Incipient mantle delamination, active tectonics and crustal thickening in Northern Morocco: Insights from gravity data and numerical modeling. *Earth and Planetary Science Letters*, *454*, 113–120.

Bargach, K., Ruano, P., Chabli, A., Galindo-ZaldÍvar, J., Chalouan, A., Jabaloy, A., et al. (2004). Recent tectonic deformations and stresses in the frontal part of the Rif Cordillera and the Saïss Basin (Fes and Rabat regions, Morocco). *Pure and Applied Geophysics*, *161*(3), 521–540.

Bendkik, A., Chenakeb, M., El Youssfi, H., Kerzazi, K., Valleri, G., & Lamdaouar, K. (2004). Carte géologique du Maroc, Sidi Kacem, échelle, (Map 1:50000). Service géologique du Maroc, Notes et mémoires

Bernard, M., Decluseau, D., Gabet, L., & Nonin, P. (2012). 3D capabilities of Pleiades satellite. International archives of the photogrammetry. *Remote Sensing and Spatial Information Sciences*, *39*, 553–557. https://doi.org/10.5194/isprsarchives-XXXIX-B3-553-201

Bezada, M. J., Humphreys, E. D., Toomey, D. R., Harnafi, M., Dávila, J. M., & Gallart, J. (2013). Evidence for slab rollback in westernmost Mediterranean from improved upper mantle imaging. *Earth and Planetary Science Letters*, *368*, 51–60.

Blanc, P.-L. (2009). Earthquakes and Tsunami in November 1755 in Morocco: A different reading of contemporaneous documentary sources. *Natural Hazards & Earth System Sciences*, *9*, 725–738. https://doi.org/10.5194/nhess-9-725-2009

Borchers, B., Marrero, S., Balco, G., Caffee, M., Goehring, B., Lifton, N., et al. (2016). Geological calibration of spallation production rates in the CRONUS-Earth project. *Quaternary Geochronology*, *31*, 188–198. https://doi.org/10.1016/j.quageo.2015.01.009

Braucher, R., Del Castillo, P., Siame, L., Hidy, A. J., & Bourlès, D. L. (2009). Determination of both exposure time and denudation rate from an in situ-produced ^{10}Be depth profile: A mathematical proof of uniqueness. Model sensitivity and applications to natural cases. *Quaternary Geochronology*, *4*(1), 56–67.

Braucher, R., Guillou, V., Bourlès, D. L., Arnold, M., Aumaître, G., Keddadouche, K., & Nottoli, E. (2015). Preparation of ASTER in-house ^{10}Be/^{9}Be standard solutions. *Nuclear Instruments and Methods in Physics Research B*, *361*, 354–360.

Braucher, R, Keddadouche, K., Aumaître, G., Bourlès, D. L, Arnold, M., & Pivot, S. (2018). Chlorine measurements at the 5MV French AMS national facility ASTER: Associated external uncertainties and comparability with the 6MV DREAMS facility. *Nuclear Instruments and Methods in Physics Research Section B: Beam Interactions with Materials and Atoms*, *420*, 40–45. https://doi.org/10.1016/j.nimb.2018.01.025

Braucher, R., Merchel, S., Borgomano, J., & Bourlès, D. (2011). Production of cosmogenic radionuclides at great depth: A multi element approach. *Earth and Planetary Science Letters*, *309*(1–2), 1–9. https://doi.org/10.1016/j.epsl.2011.06.036

Brown, E. T., Edmond, J. M., Raisbeck, G. M., Yiou, F., Kurz, M. D., & Brook, E. J. (1991). Examination of surface exposure ages of Antarctic moraines using in situ produced ^{10}Be and ^{26}Al. *Geochimica et Cosmochimica Acta*, *55*(8), 2269–2283. https://doi.org/10.1016/0016-7037(91)90103-C

Carte Néotectonique du Maroc. (1994). Echelle l/1000000, Feuille 1: Provinces du Nord. Royaume du Maroc, Ministère de 1'Energie et des Mines, Direction de la Géologie, Editions du Service Géologique du Maroc.

Chalouan, A., Gil, A. J., Galindo-Zaldívar, J., Ahmamou, M., Ruano, P., de Lacy, M. C., et al. (2014). Active faulting in the frontal Rif Cordillera (Fez region, Morocco): Constraints from GPS data. *Journal of Geodynamics*, *77*, 110–122. https://doi.org/10.1016/j.jog.2014.01.002

Chalouan, A., Michard, A., El Kadiri, K., Negro, F., De Lamotte, D. F., Soto, J. I., & Saddiqi, O. (2008). The Rif belt. In *Continental evolution: The geology of Morocco* (pp. 203–302). Berlin, Heidelberg: Springer.

Chalouan, A., Michard, A., Feinberg, H., Montigny, R., & Saddiqi, O. (2001). The Rif mountain building (Morocco); a new tectonic scenario. *Bulletin de la Société géologique de France*, *172*(5), 603–616. https://doi.org/10.2113/172.5.603

Chenakeb, M., Bendkik, A., & Zouibaa, A. (2004). Carte géologique du Maroc, Beni Ammar. échelle, (Map 1:50000). Service géologique du Maroc, Notes et mémoires.

Cherkaoui, T. (1991). Contribution à l'étude de l'aléa sismique au maroc: Le séisme d'Agadir (29/02/1960) et la microsismicité d'Al Hoceima (PhD, Université de Grenoble). Grenoble.

Cherkaoui, T., & Asebriy, L. (2003). Le risque sismique dans le Nord du Maroc. Travaux de l'Institut Scientifique. *Série Géologie et Géographie Physique*, *21*, 225–232.

Cherkaoui, T., & Medina, F. (1988). Révision des données macrosismiques et du mécanisme au foyer du séisme d' Agadir du 29 février 1960. *Revue de Géographie du Maroc*, *12*, 51–61.

Cherkaoui, T., Medina, F., & Mridekh, A. (2017). Re-examination of the historical 11 May, 1624 Fez earthquake parameters. *Fisica de la Tierra*, *29*, 135–157. https://doi.org/10.5209/FITE.57469

Chmeleff, J., von Blanckenburg, F., Kossert, K., & Jakob, D. (2010). Determination of the ^{10}Be half-life by multicollector ICP-MS and liquid scintillation counting. *Nuclear Instruments and Methods in Physics Research, Section B: Beam Interactions with Materials and Atoms*, *268*(2), 192–199. https://doi.org/10.1016/j.nimb.2009.09.012

Choubert, G., & Faure-Muret, A. (1962). Evolution du domaine atlasique marocain depuis les temps paléozoïques. *Livre Mém Fallot Mém Geol France*, *1*, 447–527.

D'Arcy, M., Schildgen, T., Turowski, J., & DiNezio, P. (2019). Inferring the timing of abandonment of aggraded alluvial surfaces dated with cosmogenic nuclides. *Earth Surface Dynamics*, *7*, 755–771.

Delunel, R., Beek, P. A., Bourlès, D. L., Carcaillet, J., & Schlunegger, F. (2014). Transient sediment supply in a high-altitude Alpine environment evidenced through a ^{10}Be budget of the Etages catchment (French Western Alps). *Earth Surface Processes and Landforms*, *39*(7), 890–899.

DeMets, C., Gordon, R. G., & Argus, D. F. (2010). Geologically current plate motions. *Geophysical Journal International*, *181*(1), 1–80.
De Reu, J., Bourgeois, J., Bats, M., Zwertvaegher, A., Gelorini, V., De Smedt, P., et al. (2013). Application of the topographic position index to heterogeneous landscapes. *Geomorphology*, *186*, 39–49.
de Vicente, G. D., Cloetingh, S., Muñoz-Martín, A., Olaiz, A., Stich, D., Vegas, R., et al. (2008). Inversion of moment tensor focal mechanisms for active stresses around the microcontinent Iberia: Tectonic implications. *Tectonics*, *27*, TC1009. https://doi.org/10.1029/2006TC002093
Dunai, T. (2010). *Cosmogenic nuclides: Principles, concepts and applications in the Earth surface sciences*. (pp. 1–187). Cambridge, UK: Cambridge University Press.
Dziewonski, A. M., Chou, T. A., & Woodhouse, J. H. (1981). Determination of earthquake source parameters from waveform data for studies of global and regional seismicity. *Journal of Geophysical Research*, *86*, 2825–2852. https://doi.org/10.1029/JB086iB04p02825
Ekström, G., Nettles, M., & Dziewonski, A. M. (2012). The global CMT project 2004-2010: Centroid-moment tensors for 13,017 earthquakes. *Physics of the Earth and Planetary Interiors*, *200-201*, 1–9. https://doi.org/10.1016/j.pepi.2012.04.002
El Alami, O., Medina, F., & Jebli, F. (1992). Etude du séisme d'Agadir du 5 avril 1992. *GAIA - Ecological Perspectives on Science and Society*, *5*, 1–5.
El Alami, O., Tadili, B. A., Cherkaoui, T. E., Médina, F., Ramdani, M., Aït Brahim, L., & Harnafi, M. (1998). The Al Hoceima earthquake of May 26, 1994 and its aftershocks: A seismotectonic study. *Annali di Geofisica*, *41*, 519–537. https://doi.org/10.4401/ag-3801
El Mrabet, T. A. (2005). Les grands séismes dans la région maghrébine, Thése d'état, Faculté des lettres et des sciences humaines, *Université Mohammed V. Rabat*, 435p. (in arabe).
Etheve, N., Frizon de Lamotte, D., Mohn, G., Martos, R., Roca, E., & Blanpied, C. (2016). Extensional vs contractional Cenozoic deformation in Ibiza (Balearic Promontory, Spain): Integration in the West Mediterranean back-arc setting. *Tectonophysics*, *682*, 35–55.
Faccenna, C., Piromallo, C., Crespo-Blanc, A., Jolivet, L., & Rossetti, F. (2004). Lateral slab deformation and the origin of the western Mediterranean arcs. *Tectonics*, *23*, TC1012. https://doi.org/10.1029/2002TC001488
Fadil, A., Vernant, P., McClusky, S., Reilinger, R., Gomez, F., Sari, D. B., et al. (2006). Active tectonics of the western Mediterranean: Geodetic evidence for rollback of a delaminated subcontinental lithospheric slab beneath the Rif Mountains, Morocco. *Geology*, *34*(7), 529–532.
Faugères, J. C. (1978). *Les rides sud-rifaines: Evolution sédimentaire et structurale d'un bassin atlantico-mésogéen de la marge africaine* (p. 480 (inédit)) (Doctoral dissertation, Thése de doctorat d'Etat). Université de Bordeaux: Bordeaux, France.
Frizon de Lamotte, D., Crespo-Blanc, A, Saint-Bézar, B., Comas, M., Fernandez, M., Zeyen, H., et al. (2004). TRANSMED Transect I: Iberian Meseta–Guadalquivir Basin–Betic Cordillera–Alboran Sea–Rif–Moroccan Meseta–High Atlas–Sahara Platform. In W. Cavazza & G. M. Stampfli (Eds.), *The TRANSMED Atlas: The Mediterranean Region from Crust to Mantle* (p. 141). Berlin: Springer.
Fukao, Y. (1973). Thrust faulting at a lithospheric plate boundary, the Portugal earthquake of 1969. *Earth and Planetary Science Letters*, *18*, 205–216.
Galbis Rodriguez, J. (1932). Catalogo sismico de la zona comprendida entre los meridianos 5°E y 20°W de Greenwich y los paralelos 45° y 25°N, tomo I. In *Instituto geográfico y catastral ed*. Madrid.
Galbis Rodriguez, J. (1940). Catalogo sismico de la zona comprendida entre los meridianos 5°E y 20°W de Greenwich y los paralelos 45° y 25°N. tomo II, In *Instituto geográfico y catastral ed*., Madrid.
Galbraith, R. F., & Green, P. F. (1990). Estimating the component ages in a finite mixture. *International Journal of Radiation Applications and Instrumentation. Part D. Tracks and Radiation Measurements*, *17*(3), 197–206. https://doi.org/10.1016/1359-0189(90)90035-V
Giaconia, F., Booth-Rea, G., Martínez-Martínez, J. M., Azañón, J. M., Pérez-Peña, J. V., Pérez-Romero, J., & Villegas, I. (2012). Geomorphic evidence of active tectonics in the Sierra Alhamilla (eastern Betics, SE Spain). *Geomorphology*, *145*, 90–106.
Gimeno-Vives, O., de Lamotte, D. F., Leprêtre, R., Haissen, F., Atouabat, A., & Mohn, G. (2020). The structure of the Central-Eastern External Rif (Morocco); Poly-phased deformation and role of the under-thrusting of the North-West African paleo-margin. *Earth-Science Reviews*, *205*, 103198.
Gosse, J. C., & Phillips, F. M. (2001). Terrestrial in situ cosmogenic nuclides: Theory and application. *Quaternary Science Reviews*, *20*, 1475–1560.
Granger, D. E., & Muzikar, P. F. (2001). Dating sediment burial with in situ-produced cosmogenic nuclides: Theory, techniques, and limitations. *Earth and Planetary Science Letters*, *188*(1–2), 269–281.
Gutscher, M. A. (2004). What caused the great Lisbon earthquake? *Science*, *305*(5688), 1247–1248.
Gutscher, M. A., Baptista, M. A., & Miranda, J. M. (2006). The Gibraltar Arc seismogenic zone (part 2): Constraints on a shallow east dipping fault plane source for the 1755 Lisbon earthquake provided by tsunami modeling and seismic intensity. *Tectonophysics*, *426*(1–2), 153–166.
Hanks, T. C., & Kanamori, H. (1979). A moment magnitude scale. *Journal of Geophysical Research*, *84*(B5), 2348–2350. https://doi.org/10.1029/JB084iB05p02348
Hatzfeld, D., & Frogneux, M. (1981). Intermediate depth seismicity in the western Mediterranean unrelated to subduction of oceanic lithosphere. *Nature*, *292*, 443–445. https://doi.org/10.1038/292443a0
International Seismological Centre. (2020). On-line Bulletin. https://doi.org/10.31905/D808B830
Johnston, A. C. (1996). Seismic moment assessment of earthquakes in stable continental regions—III. New Madrid 1811–1812, Charleston 1886 and Lisbon 1755. *Geophysical Journal International*, *126*(2), 314–344.
Jomard, H., Cushing, E. M., Palumbo, L., Baize, S., David, C., & Chartier, T. (2017). Transposing an active fault database into a seismic hazard fault model for nuclear facilities–Part 1: Building a database of potentially active faults (BDFA) for metropolitan France. *Natural Hazards and Earth System Sciences*, *17*(9), 1573–1584.
Korschinek, G., Bergmaier, A., Dillmann, I., Faestermann, T., Gerstmann, U., Knie, K., et al. (2009). Determination of the ^{10}Be half-life by hi-ERD and liquid scintillation counting. *Geochimica et Cosmochimica Acta*, *73*, A685.
Koulali, A., Ouazar, D., Tahyat, A., King, R. W., Vernant, P., Reilinger, R. E., et al. (2011). New GPS constraints on active deformation along the Africa-Iberia Plate Boundary. *Earth and Planetary Science Letters*, *308*, 211–217.
Lal, D. (1991). Cosmic ray labeling of erosion surfaces: In situ nuclide production. *Earth and Planetary Science Letters*, *104*, 424–439. https://doi.org/10.1016/0012-821X(91)90220-C
Landgraf, A., Kübler, S., Hintersberger, E., & Stein, S. (2017). Active tectonics, earthquakes and palaeoseismicity in slowly deforming continents. *Geological Society, London, Special Publications*, *432*(1), 1–12.
Lindsay, J. B. (2016). Whitebox GAT: A case study in geomorphometric analysis. *Computers & Geosciences*, *95*, 75–84. https://doi.org/10.1016/j.cageo.2016.07.003
Lindsay, J. B., Cockburn, J. M. H., & Russell, H. A. J. (2015). An integral image approach to performing multi-scale topographic position analysis. *Geomorphology*, *245*, 51–61.

Makhubela, T. V., Kramers, J. D., Scherler, D., Wittmann, H., Dirks, P. H. G. M., & Winkler, S. R. (2019). Effects of long soil surface residence times on apparent cosmogenic nuclide denudation rates and burial ages in the Cradle of Humankind, South Africa. *Earth Surface Processes and Landforms*, *44*(15), 2968–2981.

Martinez-Solares, J. M., Arroyo, A. L., & Mezcua, J. (1979). Isoseismal map of the 1755 Lisbon earthquake obtained from Spanish data. *Tectonophysics*, *53*(3–4), 301–313.

Matias, L. M., Cunha, T., Annunziato, A., Baptista, M. A., & Carrilho, F. (2013). Tsunamigenic earthquakes in the Gulf of Cadiz: Fault model and recurrence. *Natural Hazards and Earth System Science*, *13*(1), 1–13. https://doi.org/10.5194/nhess-13-1-2013

McClusky, S., Reilinger, R., Mahmoud, S., Ben Sari, D., & Tealeb, A. (2003). GPS constraints on Africa (Nubia) and Arabia plate motions. *Geophysical Journal International*, *155*(1), 126–138.

Medina, F., & Cherkaoui, T. (1992). Mécanismes au foyer des séismes du Maroc et des régions voisines (1959 – 1986). Conséquences tectoniques. *Eclogae Geologicae Helvetiae*, *85/5*, 433–457.

Merchel, S., Arnold, M., Aumaître, G., Benedetti, L., Bourlès, D. L., Braucher, R., et al. (2008). Towards more precise ^{10}Be and ^{36}Cl data from measurements at the 10^{-14} level: Influence of sample preparation. *Nuclear Instruments and Methods in Physics Research, Section B: Beam Interactions with Materials and Atoms*, *266*(22), 4921–4926.

Merchel, S., & Bremser, W. (2004). First international ^{26}Al interlaboratory comparison – Part I. *Nuclear Instruments and Methods in Physics Research, Section B: Beam Interactions with Materials and Atoms*, *223-224*, 393–400. https://doi.org/10.1016/j.nimb.2004.04.076

Merchel, S., Bremser, W., Alfimov, V., Arnold, M., Aumaître, G., Benedetti, L., et al. (2011). Ultra-trace analysis of ^{36}Cl by accelerator mass spectrometry: An interlaboratory study. *Analytical and Bioanalytical Chemistry*, *400*(9), 3125–32. https://doi.org/10.1007/s00216-011-4979-2

Merchel, S., & Herpers, U. (1999). An update on radiochemical separation techniques for the determination of long-lived radionuclides via accelerator mass spectrometry. *Radiochimica Acta*, *84*(4), 215–220.

Michard, A., Chalouan, A., Feinberg, H., Goffé, B., & Montigny, R. (2002). How does the alpine belt end between Spain and Morocco? *Bulletin de la Soci´et´e g´eologique de France*, *173*(1), 3–15. https://doi.org/10.2113/173.1.3

Michard, A., Saddiqi, O., Chalouan, A., & Frizon de Lamotte, D. (2008). *Continental evolution: The geology of morocco. Structure, stratigraphy, and tectonics of the Africa-Atlantic-Mediterranean triple junction*. Lecture Notes in Earth Sciences, (Vol. 116), Berlin Heidelberg: Springer-Verlag.

Moratti, G., Piccardi, L., Vannucci, G., Belardinelli, M. E., Dahmani, M., Bendkik, A., & Chenakeb, M. (2003). The 1755 "Meknes" earthquake (Morocco): Field data and geodynamic implications. *Journal of Geodynamics*, *36*(1–2), 305–322.

Morel, J. L. (1988). Evolution récente de l'orogène rifain et de son avant pays depuis la fin de la mise en place des nappes (Rif-Maroc). *Geodiffusion*, *4*, 584.

Morel, J. L. (1989). Etats de contrainte et cinématique de la chaîne rifaine (Maroc) du Tortonien à l'actuel. *Geodynamica Acta*, *3*, 238–294.

Morel, J. L., & Meghraoui, M. (1996). Goringe-Alboran-Tell tectonic zone: A transpression system along the Africa-Eurasia plate boundary. *Geology*, *24*(8), 755–758.

Moreno, B., Atakan, K., Furuløkken, K. A., Temel, S., & Berland, O. J. (2004). SAFE-tools: A web-based application for identification of active faults. *Seismological Research Letters*, *75*(2), 205–213.

Moulin, A., Benedetti, L., Rizza, M., Jamšek Rupnik, P., Gosar, A., Bourlès, D., et al. (2016). The Dinaric fault system: Large-scale structure, rates of slip, and Plio-Pleistocene evolution of the transpressive northeastern boundary of the Adria microplate. *Tectonics*, *35*(10), 2258–2292. https://doi.org/10.1002/2016TC004188

Mourabit, T., Abou Elenean, K. M., Ayadi, A., Benouar, D., Ben Suleman, A., Bezzeghoud, M., et al. (2014). Neo-deterministic seismic hazard assessment in North Africa. *Journal of Seismology*, *18*(2), 301–318. https://doi.org/10.1007/s10950-013-9375-2

Nishiizumi, K. (2004). Preparation of ^{26}Al AMS standards. *Nuclear Instruments and Methods in Physics Research, Section b: Beam Interactions with Materials and Atoms*, *223-224*, 388–392. https://doi.org/10.1016/j.nimb.2004.04.075

Nishiizumi, K., Imamura, M., Caffee, M. W., Southon, J. R., Finkel, R. C., & McAninch, J. (2007). Absolute calibration of ^{10}Be AMS standards. *Nuclear Instruments and Methods in Physics Research, Section B: Beam Interactions with Materials and Atoms*, *258*(2), 403–413. https://doi.org/10.1016/j.nimb.2007.01.297

Owen, L. A., Frankel, K. L., Knott, J. R., Reynhout, S., Finkel, R. C., Dolan, J. F., & Lee, J. (2011). Beryllium-10 terrestrial cosmogenic nuclide surface exposure dating of Quaternary landforms in Death Valley. *Geomorphology*, *125*(4), 541–557.

Panagiotakis, E., Chrysoulakis, N., Charalampopoulou, V., & Poursanidis, D. (2018). Validation of Pleiades Tri-Stereo DSM in urban areas. *ISPRS International Journal of Geo-Information*, *7*(3), 118.

Peláez, J. A., Chourak, M., Tadili, B. A., Aït Brahim, L., Hamdache, M., López Casado, C., & Martínez Solares, J. M. (2007). A catalog of main Moroccan earthquakes from 1045 to 2005. *Seismological Research Letters*, *78*(6), 614–621. https://doi.org/10.1785/gssrl.78.6.614

Pereira De Sousa, F. L. (1919). O Terremoto Do 1 De Novembro De 1755 Em Portugal E Um Estudo Demográfico. Serviços Geológicos, Lisbon, Portugal.

Pérouse, E., Vernant, P., Chéry, J., Reilinger, R., & McClusky, S. (2010). Active surface deformation and sub-lithospheric processes in the western Mediterranean constrained by numerical models. *Geology*, *38*(9), 823–826.

Poujol, A., Ritz, J. F., Tahayt, A., Vernant, P., Condomines, M., Blard, P. H., et al. (2014). Active tectonics of the Northern Rif (Morocco) from geomorphic and geochronological data. *Journal of Geodynamics*, *77*, 70–88.

Poujol, A., Ritz, J. F., Vernant, P., Huot, S., Maate, S., & Tahayt, A. (2017). Which fault destroyed Fes city (Morocco) in 1755? A new insight from the Holocene deformations observed along the southern border of Gibraltar arc. *Tectonophysics*, *712–713*, 303–311. https://doi.org/10.1016/j.tecto.2017.05.036

Ritz, J. F., Baize, S., Ferry, M., Larroque, C., Audin, L., Delouis, B., & Mathot, E. (2020). Surface rupture and shallow fault reactivation during the 2019 Mw 4.9 Le Teil earthquake, France. *Communications Earth & Environment*, *1*(1), 1–11.

Rizza, M., Abdrakhmatov, K., Walker, R., Braucher, R., Guillou, V., Carr, A. S., et al. (2019). Rate of slip from multiple Quaternary dating methods and paleoseismic investigations along the Talas-Fergana Fault: Tectonic implications for the Tien Shan Range. *Tectonics*, *38*(7), 2477–2505. https://doi.org/10.1029/2018TC005188

Roux, G. (1934). Notes sur les tremblements de terre ressentis au Maroc avant 1933. *Mémoire de la Société Scientifique Nationale du Maroc*, *39*, 42–71.

Rupnik, E., Pierrot-Deseilligny, M., & Delorme, A. (2018). 3D reconstruction from multi-view VHR-satellite images in MicMac. *ISPRS Journal of Photogrammetry and Remote Sensing*, *139*, 201–211. https://doi.org/10.1016/j.isprsjprs.2018.03.016

Ryerson, F. J., Tapponnier, P., Finkel, R. C., Meriaux, A.-S., Van der Woerd, J., Lasserre, C., et al. (2006). Applications of morphochronology to the active tectonics of Tibet. In L. L. Siame, D. L. Bourlès, & E. T. Brown (Eds.), (Eds). *In situ-produced cosmogenic nuclides and quantification of geological processes: Geological Society of America Special Paper 415* (pp. 61–86). https://doi.org/10.1130/2006.2415(05)

Sani, F., Del Ventisette, C., Montanari, D., Bendkik, A., & Chenakeb, M. (2007). Structural evolution of the Rides Prerifaines (Morocco): Structural and seismic interpretation and analogue modelling experiments. *International Journal of Earth Sciences*, *96*(4), 685–706.

Schimmelpfennig, I., Benedetti, L., Finkel, R., Pik, R., Blard, P.-H., Bourlès, D., et al. (2009). Sources of in-situ ^{36}Cl in basaltic rocks. Implications for calibration of production rates. *Quaternary Geochronology*, *4*(6), 441–461. https://doi.org/10.1016/j.quageo.2009.06.00

Sébrier, M., Siame, L., Zouine, E. M., Winter, T., Missenard, Y., & Leturmy, P. (2006). Active tectonics in the Moroccan High Atlas. *Comptes Rendus - Geoscience*, *338*(1–2), 65–79. https://doi.org/10.1016/j.crte.2005.12.001

Siame, L. L., Chen, R. F., Derrieux, F., Lee, J. C., Chang, K. J., Bourlès, D. L., et al. (2012). Pleistocene alluvial deposits dating along frontal thrust of Changhua Fault in western Taiwan: The cosmic ray exposure point of view. *Journal of Asian Earth Sciences*, *51*, 1–20.

Siame, L. L., & Sébrier, M. (2004). Determination of a basic set of diagnostic criteria to identify and characterize slow active faults. Deliverable Re9.3 (WP9: Criteria for characterizing slow active faults and standardization of paleoseismological analyses) of S.A.F.E. Project (European Project EVG1-2000-22005). Retrieved from https://www.researchgate.net/publication/233944555_Siame_LL_and_Sebrier_M_2004_Determination_of_a_basic_set_of_diagnositic_criteria_to_identify_and_characterise_slow_active_faults_Deliverable_Re93_Workpackage9_Criteria_for_characterising_slow_active_f

Stone, J. O. (2000). Air pressure and cosmogenic isotope production. *Journal of Geophysical Research*, *105*(B10), 23753–23759. https://doi.org/10.1029/2000JB90018

Suter, G. (1980). Carte géologique/structurale de la chaîne rifaine, échelle, 1:500000. Service des Cartes géologiques, Maroc.

Takaku, J., Tadono, T., Tsutsui, K., & Ichikawa, M. (2014). Validation of 'AW3D' Global DSM Generated from Alos Prism. *ISPRS Annals of the Photogrammetry, Remote Sensing and Spatial Information Sciences*, *III-4*, 25–31.

Takaku, J., Tadono, T., Tsutsui, K., & Ichikawa, M. (2018). *Quality improvements of 'AW3D'Global DSM derived from ALOS PRISM*. In Proceedings of IGARSS 2018 (pp. 1612–1615). Valencia, Spain: IEEE.

Thiebot, E., & Gutscher, M. A. (2006). The Gibraltar Arc seismogenic zone (part 1): Constraints on a shallow east dipping fault plane source for the 1755 Lisbon earthquake provided by seismic data, gravity and thermal modeling. *Tectonophysics*, *426*(1–2), 135–152.

Thingbaijam, K. K. S., Martin Mai, P., & Goda, K. (2017). New empirical earthquake source-scaling laws. *Bulletin of the Seismological Society of America*, *107*(5), 2225–2246. https://doi.org/10.1785/0120170017

Vermeesch, P. (2012). On the visualisation of detrital age distributions. *Chemical Geology*, *312–313*, 190–194. https://doi.org/10.1016/j.chemgeo.2012.04.021

Vernant, P., Fadil, A., Mourabit, T., Ouazar, D., Koulali, A., Davila, J. M., et al. (2010). Geodetic constraints on active tectonics of the Western Mediterranean: Implications for the kinematics and dynamics of the Nubia-Eurasia plate boundary zone. *Journal of Geodynamics*, *49*(3–4), 123–129. https://doi.org/10.1016/j.jog.2009.10.007

Vogt, J. (1984). Mouvements de terrain associés aux séismes en Afrique du Nord. *Méditerranée*, *51*(1), 43–48.

Wells, D. L., & Coppersmith, K. J. (1994). New empirical relationships among magnitude, rupture length, rupture width, rupture area, and surface displacement. *Bulletin of the seismological Society of America*, *84*(4), 974–1002.

Wilson, J. P., & Gallant, J. C. (2000). Digital terrain analysis. *Terrain Analysis: Principles and Applications*, *6*(12), 1–27.

Zizi, M. (1996). Triassic-Jurassic extension and Alpine inversion in northern Morocco. *Mémoires du Muséum National d'histoire Naturelle*, *170*, 87–101.